Entry System Design Considerations for Mars Landers

Lockwood, Powell, NASA/LaRC; Graves, Carman, NASA/JSC

Proposed Abstract for AAS Guidance and Control Conference
Breckenridge, CO Feb. 1-4, 2001

The objective for the next generation of Mars landers is to enable a safe landing at specific geological features of scientific interest. To meet this goal requires precision landing (<10km) with the capability to perform local hazard avoidance maneuvers. This is in contrast to the first generation of Mars landers, ex. Viking and Pathfinder, which have provided successful landing on Mars, but by design, were limited to large scale (100s of kms) landing sites with limited local hazards.

The primary technology, that enables more than an order of magnitude reduction in landing footprint for the next generation lander, is guided aeromaneuvering during the entry phase of flight. This phase begins at Mars atmospheric interface and continues to supersonic parachute deploy. Local hazard avoidance is accomplished by combining active terrain sensing with guidance through the powered descent phase of flight. This phase begins when the lander jettisons the parachute to touch down.

This paper will focus on the entry phase of flight, but will describe the impacts on the other phases of flight. It will discuss the design parameters, such as ballistic coefficient, lift to drag ratio, etc that must be considered in the development of the next generation entry system. It will include the sensitivity of these parameters to landing site location and elevation, delivery accuracy, atmospheric and aerodynamic uncertainties. The impact of the design parameters on performance margins will also be discussed. This paper will give an example of how this process leads to effective aeroshell concepts that meet the next generation requirements.

AAS 01-023

American Astronautical Society

Entry System Design Considerations for Mars Landers

Mary Kae Lockwood
Richard W. Powell
NASA Langley Research Center

Claude A. Graves
Gilbert L. Carman
NASA Johnson Space Center

24th ANNUAL AAS GUIDANCE AND CONTROL CONFERENCE

January 31 - February 4, 2001
Sponsored by
Breckenridge, Colorado
Rocky Mountain Section

AAS Publications Office, P.O. Box 28130 - San Diego, California 92198

AAS 01-023

ENTRY SYSTEM DESIGN CONSIDERATIONS FOR MARS LANDERS

Mary Kae Lockwood
Richard W. Powell
NASA Langley Research Center

Claude A. Graves
Gilbert L. Carman
NASA Johnson Space Center

INTRODUCTION

The objective for the next generation of Mars landers is to enable a safe landing at specific locations of scientific interest. The 1st generation entry, descent and landing systems, ex. Viking and Pathfinder, provided successful landing on Mars but by design were limited to large scale, 100s of km, landing sites with minimal local hazards. The 2nd generation landers, or smart landers, will provide scientists with access to previously unachievable landing sites by providing precision landing to less than 10 km of a target landing site, with the ability to perform local hazard avoidance, and provide hazard tolerance. This 2nd generation EDL system can be utilized for a range of robotic missions with vehicles sized for science payloads from the small 25-70 kg, Viking, Pathfinder, Mars Polar Lander and Mars Exploration Rover-class, to the large robotic Mars Sample Return, 300 kg plus, science payloads.[1] The 2nd generation system can also be extended to a 3rd generation EDL system with pinpoint landing, 10's of meters of landing accuracy, for more capable robotic or human missions. This paper will describe the design considerations for 2nd generation landers. These landers are currently being developed by a consortium of NASA centers, government agencies, industry and academic institutions. The extension of this system and additional considerations required for a 3rd generation human mission to Mars will be described.

SYMBOLS/NOMENCLATURE

AFE	Aeroassist Flight Experiment	
AGL	Altitude Above Ground Level	
CFD	Computational Fluid Dynamics	
cg	center of gravity location	m
C_L	lift coefficient (lift/q S)	
C_D	drag coefficient (drag/q S)	
C_m	pitching moment coefficient (pitching moment/q S l)	
C_{m_α}	$\delta C_m/\delta\alpha$	deg^{-1}
D	sensed drag	N
D_{ref}	reference drag	N
EDL	Entry, Descent and Landing	
ETPC	Entry Terminal Point Controller	
g	acceleration due to gravity	m/s^2
g_s	acceleration due to gravity at Mars surface	m/s^2
h	altitude	m
IMU	Inertial Measurement Unit	
K2ROLL	direction of commanded bank angle	
K_3	over control gain	
l	reference length	m
L/D	lift to drag ratio	
L/D_c	commanded L/D	

L/D_{ref}	reference L/D	
m,M	mass	kg
MSP	Mars Surveyor Program	
NAV	state variables calculated by navigation system	
q	dynamic pressure	Pa
r	magnitude of radius vector from Mars center to spacecraft	km
r_e	Mars equatorial radius	m
r_{ref}	reference magnitude of radius vector from Mars center to spacecraft	km
R	great circle range to target	km
R_p	predicted great circle range to target	km
R_{ref}	reference great circle range to target	km
s	range	km
S	reference area	m^2
Sol	1 Martian day (≈24.6 hours)	
t	time	s
TPS	Thermal Protection System	
v	relative velocity magnitude	m/s
$x(t)$	vector of state variables	
xcg	axial cg location	m
Δaero	increment applied to mean lift and drag coefficients	
Δcg	change in spacecraft cg	m
α	trim angle of attack	deg
$\Delta\alpha$	increment added to α	deg
B_m	ballistic coefficient (M/C_DS)	kg/m^2
λ	influence coefficients	
ϕ_c	commanded bank angle	deg
γ	relative flight path angle	deg
γ_I	inertial flight path angle	deg
ρ	atmospheric density	kg/m^3
ρ_{mean}	mean atmospheric density	kg/m^3

2ND GENERATION EDL SYSTEM DESCRIPTION

An illustration of a representative 2nd generation lander system concept is provided in Figure 1. The entry capsule pictured is being designed for both direct entry, as has been done in the recent Mars Pathfinder mission, or delivery into the atmosphere from orbit, as has been done in Viking. Carrier vehicle options range from a cruise stage, to an orbiter spacecraft with it's own mission.

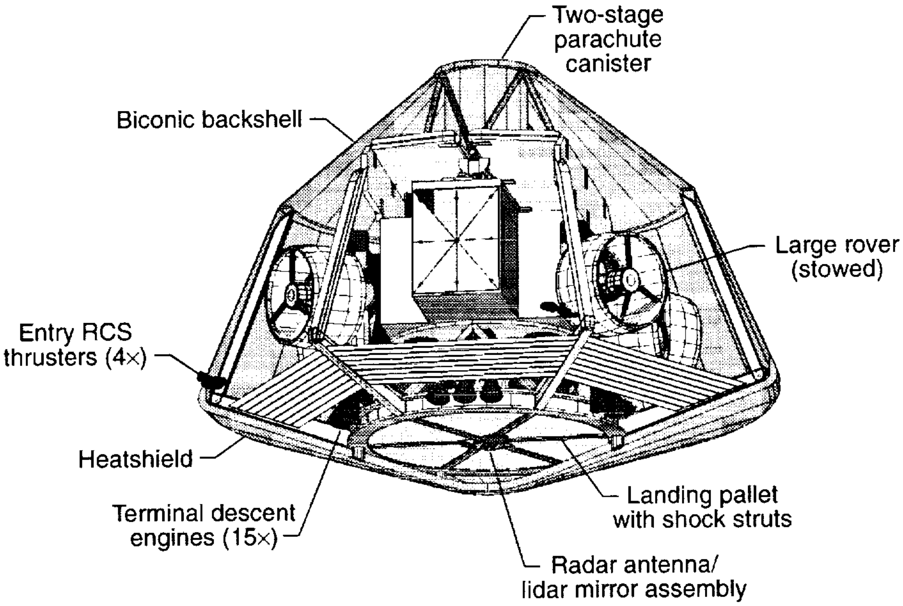

Figure 1 Entry Capsule Cutaway View

The entry capsule is designed to accommodate potentially large science payloads of 300 kg or more while providing the capability to aeromaneuver and land within ±3 km (99.7 percentile) of a designated target site. As shown in Figure 2, the launch loads are carried through the cruise stage, through the heatshield and into the lander. Due to the mass distribution of the lander, the cruise stage-heatshield attachment allows for a lower mass system compared to carrying the launch loads through the backshell for a cruise stage to backshell attachment. The biconic backshell is used to obtain high volumetric efficiency in payload packaging (a large rover is shown in Figure 1 as an example). A two-stage parachute system is employed, enabling deceleration of large spacecraft while allowing time for terminal sensing and hazard avoidance maneuvers during terminal descent. Both radar and lidar sensors are used for local terrain-relative navigation to identify safe landing sites.

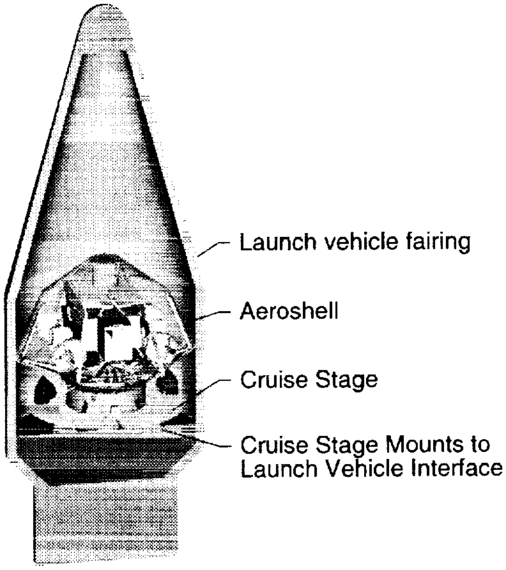

Figure 2 Launch configuration

The touchdown event itself is made as robust as possible to any residual terrain hazards. Figure 1 shows one example of a robust landing approach; a pallet-type structure augmented with webbed shock struts to help prevent tip-over. This scheme and other alternatives are discussed further by Rivellini.[2]

HUMAN MARS MISSION SYSTEM DESCRIPTION

Human exploration of Mars requires flights that deliver large masses and volumes to Mars, presently estimated to be in packages of up to about 100 mt to Mars orbit and about 60 mt to the Mars surface, in a combination of crewed and cargo flights. Even though the human missions require an increase in Mars delivered mass that is more than an order of magnitude greater than for robotic missions, many of the important aeroassist capabilities for robotic missions are also key capabilities needed for human Mars missions. Robotic missions provide an opportunity to demonstrate these key aeroassist capabilities before beginning human exploration of Mars. Common aeroassist capabilities for these two classes of missions are aerocapture to improve the efficiency of deceleration into Mars orbit, precision landing to an accuracy of 10's of meters, hazard avoidance, hazard tolerance, and autonomous aeroassist operations. Human exploration of Mars imposes significant additional aeroassist challenges that are driven primarily by safety considerations for the flight crew and the high value cargo flights, the large mass and volumes that must be transported to Mars orbit and to the Mars surface, limits on allowable aerodynamic loads, and the restrictions on transit time between earth and Mars.

Crew and cargo safety considerations require mission and safe crew return reliability that exceeds that generally provided for robotic missions. This influences system and component reliability and redundancy requirements, system performance margins, and the technology readiness that is acceptable for human missions. The flight crew has the potential for enhancing safety for the crewed missions by using human capabilities to augment the system operation and performance, however after the long journey to Mars the potential for limited crew physical capability does not permit relying on this capability. Further, the cargo flights must have autonomous aeroassist capability. The large masses and volumes needed for human missions require much larger aeroshells and related systems. These large systems present especially difficult challenges in the landing dynamics and in achieving efficient deceleration in the supersonic to subsonic flight regime, which has traditionally used a parachute deceleration system. The aerodynamic loads for human flights must be limited to no more than 5.0 g's with a desire to further limit the maximum loads to 3.5 g's. Human flights also constrain the maximum transit time to Mars to 205 days and this increases the maximum Mars entry speed to 7.36 km/s for human flights.

2ND GENERATION ROBOTIC LANDER EDL SEQUENCE OF EVENTS

The key events occurring during entry, descent, and landing are described below.

Approach Phase. Prior to entry the spacecraft must be guided to the target entry corridor. This may be accomplished either with the spacecraft's propulsion and guidance and control system or the entry capsule may be augmented with an external propulsion system, also controlled by the onboard guidance and control system.

Entry/Aeromaneuvering Phase. Once the spacecraft begins to encounter the atmosphere, the entry guidance logic is activated. The guidance system computes bank angle commands to direct the capsule's lift vector such that the correct supersonic parachute deploy conditions are achieved at a desired position relative to the target landing site. In this scheme the bank angle magnitude is used to control the total range, and the bank angle direction is used to control crossrange. This guided aeromaneuvering during entry is the 2nd generation lander technology that results in landing footprints on the Mars surface of less than 10km. This is in contrast to the unguided ballistic entrys of the 1st generation landers, which have footprints of 100s of km. The entry guidance scheme is a derivative of the Apollo entry guidance approach,[3] and has been tested extensively in a high fidelity simulation environment[4] for use at Mars. Both the simulation and guidance scheme will be discussed in more detail below.

Parachute Descent Phase. Deployment of the supersonic parachute is triggered by the entry guidance logic, discussed further below, to be within the Viking qualification box of Mach 1.6 to Mach 2.28 and dynamic pressures of 400 to 1175 Pa. This parachute is a derivative of the Mars Pathfinder mortar-deployed parachute, and serves as a drogue parachute in this EDL system, decelerating the spacecraft to subsonic velocities. Once the vehicle reaches Mach 0.8, the backshell and supersonic parachute are jettisoned (eliminating mass that is no longer needed), and a much larger subsonic main parachute is deployed to further reduce the vehicle velocity to terminal velocities of 40-50 m/sec prior to initiation of powered descent.

During parachute descent, terrain-relative navigation is initiated. The landing radar acquires position at an altitude above ground level (AGL) of 3.7 km, and velocity at an AGL of 2.1 km, allowing the onboard navigation system to accurately determine the spacecraft's surface-relative altitude and velocity. In the 1.5 to 1.0 km AGL range a scanning lidar begins periodically generating local elevation maps of the surface, in the area surrounding the guidance system's current projected landing site. The lidar elevation maps are used to identify any potential hazards near the projected site. Results are utilized by the guidance system to redesignate the target site to a safer location if necessary.

Powered Descent Phase. The lander's guidance system computes an appropriate time to separate from the subsonic parachute to initiate powered descent. This computation establishes a trajectory that will reach the designated target site.

The radar and lidar sensors, along with the hazard detection and retargeting logic, continue to operate during powered descent, scanning the target site and the surrounding area as the effective resolution of the lidar-generated terrain maps improves, redesignating the target site as needed, to avoid local hazards. The guidance system updates the commanded lander attitude to reach the current target using a set of algorithms derived from the powered descent guidance logic for the Apollo Lunar Module.[5]

Touchdown: Powered descent concludes with thrust termination approximately 1 m above the surface, resulting in velocity components at touchdown of approximately 3 m/s (vertical) and a tolerance of ±0.5 m/s (horizontal), well within the capabilities of the landing/arrest approaches under consideration.

Each of the EDL phases and corresponding vehicle subsystems are designed to achieve a soft touchdown at the design landing site elevation for the expected range of dispersions or uncertainties in delivery states at atmospheric interface, atmosphere dispersions, vehicle aerodynamics, etc. Energy at atmospheric interface is taken out in the entry, supersonic chute, subsonic chute, powered descent and landing system. The entry states, vehicle M/C_DS, gravity and atmosphere govern the altitude at which the vehicle meets the Viking parachute qualification box. For example, vehicles with larger ballistic coefficients will reach the Viking parachute qualification box at altitudes lower than vehicles with smaller ballistic coefficients for the same entry conditions and atmospheric density profile. In general the higher ballistic coefficient will shorten the parachute and powered descent event sequence and can affect the sizing of the parachute and powered descent engine systems.

SEQUENCE OF EVENTS FOR MARS HUMAN EXPLORATION MISSIONS

Human exploration of Mars, as presently envisioned, will use aeroassist for three purposes; aerocapture into Mars orbit; entry, descent, and landing (EDL) at Mars; and either a direct entry or aerocapture into the earth's atmosphere as part of the return to earth. An overall mission scenario that illustrates this aeroassist concept is shown in Figure 3. This scenario shows that two separate major cargo elements, using a single trans-Mars injection opportunity, will use aerocapture to decelerate into Mars orbits. One element consisting of a surface habitat, a power generating system, surface exploration equipment, an aeroshell, and other EDL components will aerocapture into a low energy Mars orbit. This element will remain in Mars orbit for a short period, allowing for appropriate mission operations and proper phasing with the landing site, and at the appropriate time will perform a deorbit maneuver that is followed by EDL to place the habitat, power generating, and surface exploration equipment at a pre-selected point on the Mars surface. The other element consisting of a Mars ascent vehicle, used to return to a one Sol Mars orbit after the Mars surface stay is completed, an aeroshell, and other EDL components will aerocapture into a one Sol Mars orbit. This element will remain in a one Sol Mars orbit until the arrival of the crew that injects on a fast trans-Mars trajectory on the subsequent trans-Mars injection opportunity. The element transporting the crew to Mars, which consists of a habitat for use during transit between earth and Mars, the flight crew, and an aeroshell, also uses aerocapture to decelerate into a one Sol Mars orbit. This element then executes a rendezvous with the element carrying the Mars ascent vehicle, the crew transfers into the crew module attached to the Mars ascent vehicle, and preparations begin for separation and descent to the Mars surface. At the appropriate time a deorbit maneuver is performed and that is followed by an EDL with landing near the pre-deployed surface habitat.

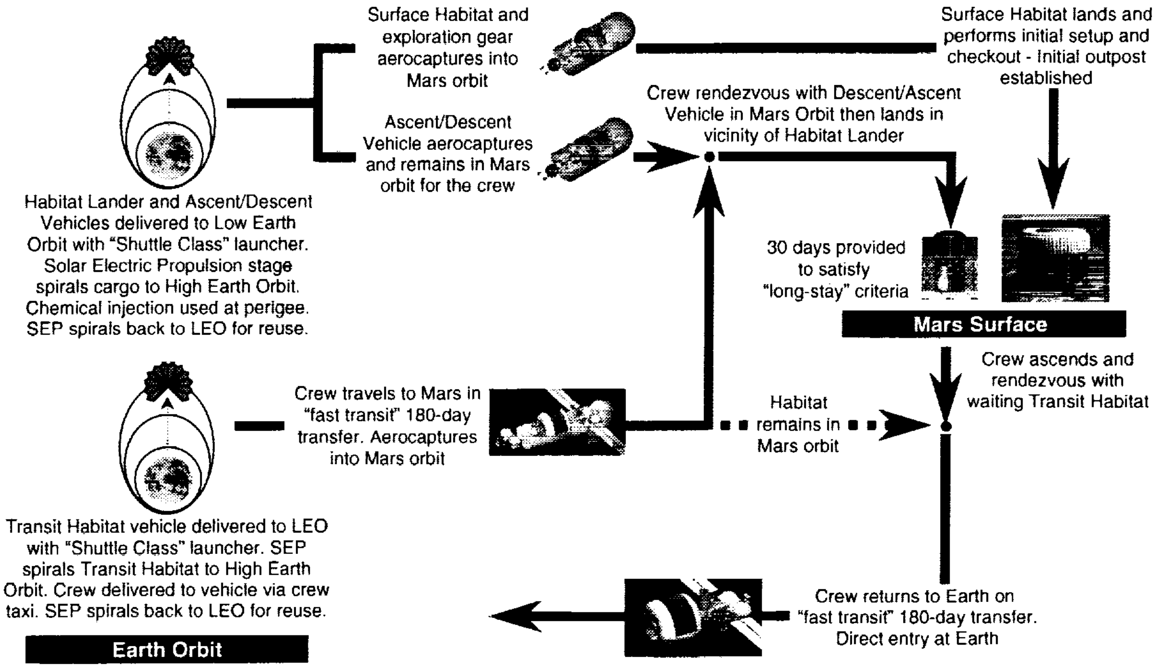

Figure 3 Mars Human Mission Overview

The EDL from Mars orbit is very similar to the EDL for the robotic missions that use direct entry. The current design of the human missions has a maximum of 205 day Earth to Mars transfer time. This constraint can increase the entry velocity at Mars over the corresponding robotic mission depending on the opportunity. Lift vector modulation is used to manage the energy dissipation and profile shaping to achieve the desired state conditions prior to deployment of low speed deceleration devices. Propulsive deceleration will be used to remove the remaining energy and to provide the terminal maneuvering needed to remove residual state errors, to avoid local surface obstacles, and to provide the proper orientation for landing. The terminal descent will be very similar to the terminal descent of soft-landed robotic missions, but with additional capability provided for the flight crew to re-designate the landing site as an additional asset for the crewed flights. The angle-of-attack prior to terminal descent is about 55 deg. so a pitch maneuver, as illustrated in Figure 4, is needed to lower the angle-of-attack prior to initiation of powered descent. The ballistic coefficient, M/C_DS, of the EDL configuration for human missions will be significantly larger than for robotic missions so improved deceleration efficiency of the supersonic to subsonic flight regime will be necessary, along with significant enlargement of the deployment envelope of aerodynamic deceleration devices during terminal descent.

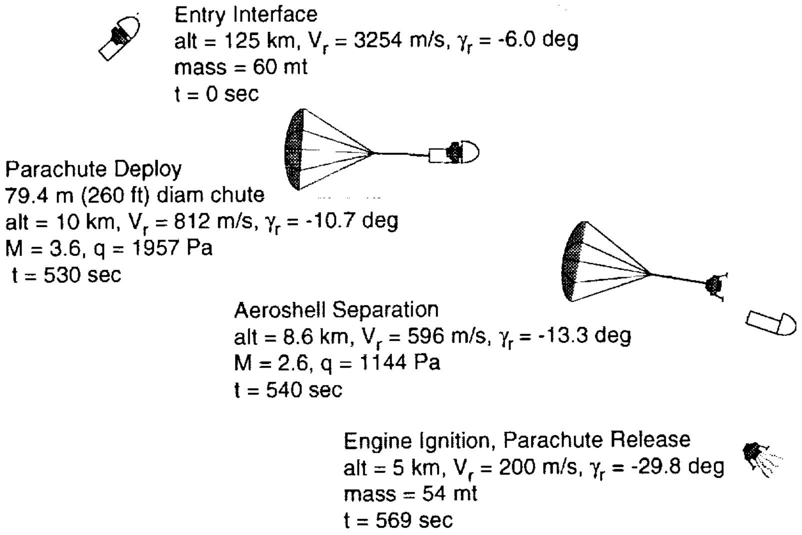

Figure 4 Mars Human Mission Entry, Descent, and Landing Scenario

SIMULATION OBJECTIVES AND DESCRIPTION

A high fidelity simulation was developed to assess the ability of the 2nd generation lander, described above, to meet the design objectives. The primary objectives are to reach the parachute deployment point within 3 km of the target, stay within the parachute qualification envelope, and touchdown safely at least 99.7% of the time. Once this assessment was completed, the simulation was used to develop recommended changes, either in mission operations or spacecraft design that would meet the mission objectives. The following sections describe the simulation, and the characteristics that were varied in the Monte Carlo analysis to assess the mission performance and risk statistics.

This simulation has evolved from simulating EDL of 1st generation systems, such as Mars Pathfinder, Mars Polar Lander and Mars Exploration Rover, and can be extended to provide simulation of 3rd generation EDL systems including human missions.

The three degree-of-freedom (3-DOF) version of the Program to Optimize Simulated Trajectories (POST)[6] is the core software for the EDL simulations. POST is used to integrate the equations of motion and provides the necessary links to the other models required for the simulation. These models include planet definition, gravity, atmosphere, aerodynamic data, control system emulation, guidance algorithms, navigation system, and mass properties. Figure 5 illustrates the basic flow of the simulation. This simulation has been coupled with a Monte Carlo executive to provide the required statistics. The following sections describe the basic simulation models, and how the vehicle and mission parameters are varied in the model to complete a Monte Carlo analysis.

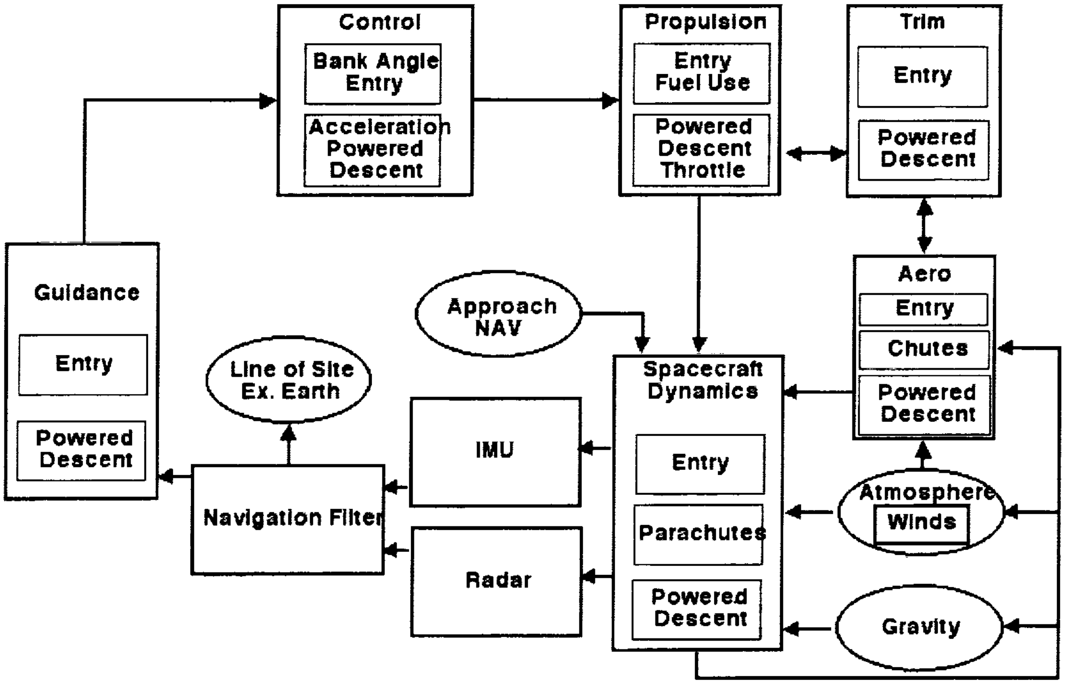

Figure 5 3-DOF Simulation

SIMULATION MODELS

Planet Model

The planet model, which models Mars as an oblate spheroid, defines the physical dimensions and characteristics of Mars. This model is used for both altitude, latitude, and longitude determinations, and to determine the Mars relative velocity vector required by the guidance algorithms and other simulation models. The Mars planetary model parameters used in the simulation are shown in Table 1.

TABLE 1

MARS PLANETARY MODEL PARAMETERS

Gravitational Parameter (μ)	$4.28282868534 \times 10^{13}$ m^3/sec^2
Equatorial Radius (r_E)	3393.940 km
Polar Radius (r_P)	3376.780 km
Mars Rotational Velocity (ω_{MARS})	7.088218×10^{-5} rad/sec

Gravity Model

The gravity model uses zonal, sectoral, and tesseral harmonic terms to determine the acceleration due to gravity. This model is a 50-by-50 Mars gravity field based on the Viking and Mariner 9 data which was also used in the Mars Pathfinder and Polar Lander Programs.[7]

Atmosphere Model

The Mars Global Reference Atmosphere Model[8] version 3.7 (MarsGRAM 3.7) is included in the simulations. MarsGRAM provides the nominal atmospheric data (temperature, density, and pressure) as well as random perturbations. The atmospheric data is a function of the spacecraft location (latitude, longitude, and altitude), date, time, and atmospheric opacity. (The Mars arrival date and f10.7-cm solar flux values reflect the period during the solar cycle in which the entry occurs.) A density scale factor was used to increase the magnitude of density perturbations.

Spacecraft Aerodynamic Model

A subroutine supplies the spacecraft's aerodynamics to POST. From atmospheric interface to parachute deployment, the routine uses an interpolation of discrete points obtained using computational fluid dynamic solutions and test data. The aerodatabase includes aerodynamic coefficients for the rarefied region of the atmosphere, the transitional regime, and for the continuum regime, from hypersonic to low supersonic Mach numbers.

While the spacecraft is on the parachute, the aerodynamic coefficients are the sum of two elements, namely the spacecraft and the parachute. The spacecraft aerodynamics is calculated as described above. Two parachute models were developed, one for the supersonic parachute and one for the subsonic parachute. For the supersonic chute the aerodynamic model approximates the parachute inflation dynamics, and includes the drag variability with Mach number. Based on the heritage from the Viking program, the supersonic chute is assumed to be qualified for deployment between a Mach of 1.6 and 2.28, and dynamic pressures between 400 and 1175 Pa. The subsonic chute model also approximates the inflation dynamics. It is currently deployed at Mach 0.8.

Control System Emulation

Since this is a 3-DOF simulation, the rotational dynamics must be estimated. This is done by the emulation of the control effectors for the various phases of the mission. For the portion of flight from atmospheric interface to parachute deployment, the spacecraft's control is provided by a reaction control system. To model a reaction control system, the simulation uses a combination of a bank acceleration model and a trim model to estimate angle-of-attack and sideslip angles. The bank model assumes that a constant bank acceleration is applied in the desired direction until the specified bank rate limit is reached. At this point the bank acceleration is set to zero until the bank rate must be arrested. The arresting phase is modeled by a constant bank deceleration until the desired bank angle is reached and the bank rate is zero. At this time the bank acceleration is set to zero. To model the angle of attack and sideslip angle variation during the mission, the spacecraft flies the angle of attack and sideslip that simultaneously produces a zero pitching moment and zero yawing moment.

While the parachutes are deployed, it is assumed that no control system is active. The current model assumes that the spacecraft maintains a zero degree angle of attack, sideslip and bank angle.

Once the spacecraft jettisons the subsonic parachute and is in the powered descent phase, the engines are throttled to provide the required total thrust while maintaining trim in both pitch and yaw moments.

Entry States

Entry states were generated by JPL using the best estimate of interplanetary navigation errors, interplanetary trajectory correction maneuver errors, and the Earth departure window for the mission. Corresponding knowledge states at the atmospheric interface were also generated for each entry. These knowledge states are based on simulated Deep Space Network radiometric data.

Navigation System

The navigation system model provides current estimates of states using models of the on-board strapdown IMU and the knowledge entry states. This model provides estimates of position and velocity to the guidance algorithm. Data generated using these outputs will be called "Nav" quantities in the discussion of the results.

Mass Properties

The mass properties used for these simulations were the best estimates of the respective systems. The mass history in the simulation follows the EDL sequence of events.

High fidelity simulations of the 2nd and 3rd generation robotic and human missions require the successful development and implementation of many models not required for the 1st generation systems. These include the on-board navigation system model, entry and terminal descent guidance and control models, sensor models required for terminal descent altitude and velocity determination, terrain simulation, hazard detection and avoidance logic, multi degree-of-freedom parachute models, etc. The 3-DOF simulation described above continues to be developed to include all of the models necessary to provide a high fidelity 3-DOF atmospheric flight simulation. In addition a 6-DOF simulation is also in progress. These simulations are being developed such that additional capability, to include atmospheric flight for 1st, 2nd, and 3rd generation robotic and human missions, can be readily accommodated.

ENTRY GUIDANCE ALGORITHM

To achieve precision landing capability in the presence of dispersions in entry interface conditions, system performance, and the Mars atmospheric environment, an active aero-maneuvering capability must be employed during the hypersonic entry phase. This maneuvering is accomplished by modulation of the vehicle roll attitude about the relative velocity vector (bank) to obtain the appropriate vertical component of aerodynamic lift which will guide the entry trajectory to the desired conditions at parachute deployment. The Mars Surveyor Program 2001 lander system development work included performance comparisons of several candidate entry guidance algorithms. The algorithm selected for flight implementation as a result of these comparisons was the Apollo-derived Entry Terminal Point Controller (ETPC) guidance. This algorithm is based on the final entry phase logic of the Apollo Command Module entry guidance, which was successfully flown on the Apollo program manned lunar return missions. The vehicle position and velocity state vectors and sensed acceleration vector are provided as guidance inputs from the navigation system, and the guidance provides the commanded bank angle to the flight control system.

Longitudinal control

The longitudinal channel logic controls the in-plane range to the desired parachute deployment target by varying the vertical component of the vehicle lift-to-drag ratio. The predicted in-plane range-to-go is obtained using linear perturbation theory with respect to a stored nominal reference trajectory. This reference trajectory is specified by drag acceleration, radial velocity, range-to-go, and the nominal vertical component of L/D as a function of relative velocity. By using the influence coefficients (partial derivatives) of the terminal range with respect to perturbations in drag acceleration and radial velocity, the predicted total range is obtained as shown in equation 1.

$$R_p = R_{ref} + \frac{\partial R}{\partial D}\left(D - D_{ref}\right) - \frac{\partial R}{\partial \dot{r}}\left(\dot{r} - \dot{r}_{ref}\right) \qquad (1)$$

The actual drag acceleration, D, is the sensed acceleration in the direction of the negative relative velocity vector. The desired vertical component of L/D required to null the error between the actual and predicted range is then calculated using the influence coefficient of terminal range with respect to vertical L/D.

$$\left(\frac{L}{D}\right)_C = \left(\frac{L}{D}\right)_{ref} + \frac{K_3\left(R - R_p\right)}{\partial R / \partial (L/D)} \tag{2}$$

The variable R is the actual great circle range-to-go to the in-plane projection of the target. The constant K_3 is referred to as the "over-control" gain, which allows amplification of the aggressiveness at which the range error is converged. The influence coefficients are pre-derived from the nominal reference trajectory and implemented by the guidance in the form of table lookups as a function of relative velocity. The derivation process for these influence coefficients is described below.

The bank angle command that will provide the desired vertical L/D is then calculated.

$$\Phi_C = \cos^{-1}\left(\frac{L/D_C}{L/D}\right) * K2ROLL \tag{3}$$

The term *L/D* in equation 3 is the total vehicle lift-to-drag ratio, which is derived by the guidance from sensed accelerometer measurements. K2ROLL is the direction of the bank angle command (±1).

Since the guidance has no control of the angle-of-attack and total L/D, there can be no explicit control of the terminal altitude. Altitude is, in effect, the independent parameter that is varied by the bank angle command to achieve the required atmospheric density and drag acceleration to explicitly control the terminal range. Therefore, the delivery altitude at parachute deployment will vary in proportion to dispersions in atmospheric density.

Lateral control

Prior to entry interface, the bank angle is commanded to a fixed value corresponding to the nominal starting vertical lift of the reference trajectory, and in the direction of the target position with respect to the relative trajectory plane. This prebank attitude is maintained until the sensed drag acceleration has increased to a level of 0.03 Earth g where closed loop guidance bank commands become active. The out-of-plane crossrange distance to the target during hypersonic aero-maneuvering is bounded by performing bank reversals. These reversals are commanded each time the target out-of-plane angle has increased to the reversal trigger value, which is a quadratic function of relative velocity. The bank reversal corridor is designed to be sufficiently narrow to allow adequate crossrange convergence to the target, but wide enough to prevent an excessive number of reversals. The direction of the bank reversal maneuver is determined by the magnitude of the bank angle command at the time of the reversal.

Since the bank reversals only bound the target crossrange within limits, a final proportional crossrange control phase is initiated at a relative velocity of approximately 1100 m/sec. At that time, the longitudinal ranging control is terminated, and the bank angle commands from then until parachute deployment are directly proportional to the relative velocity heading error to the target. The objective of this final phase is to zero out any remaining crossrange error. The effectiveness of the longitudinal ranging control is significantly reduced as the remaining time-to-go becomes small, and would result in excessive bank maneuvering. This final phase is a more effective use of the remaining maneuver capability, and provides a more stable roll attitude at parachute deployment.

Parachute deployment logic

As noted above the supersonic parachutes currently used by the Mars robotic landers have been certified for a deployment envelope of Mach number between 1.6 and 2.28, and dynamic pressure (q) between 400 and 1175 Pa. This envelope is the constraint within which the guidance must deliver the lander, in addition to achieving the smallest possible range to the target. To achieve the best precision in deployment position for dispersed cases, the actual deployment velocity is allowed to vary earlier or later than nominal, while remaining within the constraint envelope. Since the guidance has no knowledge of the true Mach number and dynamic pressure, these constraints are incorporated as limits in relative velocity and drag acceleration, respectively, with adequate margins to prevent constraint violations in the presence of dispersions.

The tests for parachute deployment begin when the relative velocity has become less than or equal to the upper limit, corresponding to Mach 2.28. The deployment is then commanded by the guidance at the first occurrence of one or more of the following three conditions.

1. Range-to-go becomes less than or equal to zero. (Positive range is defined as range short of the target)

2. Relative velocity becomes less than or equal to the lower limit (Mach = 1.6)

3. Drag acceleration becomes less than or equal to the lower limit ($q = 400$ Nt/m^2)

The guidance deployment command can occur no earlier than the upper limit of the constraint envelope (Mach 2.28), even though the target may have been overflown by then in high energy dispersed cases. Also, the deployment must occur no later than the lower limits of the constraint envelope, even though the target may not have yet been reached in low energy dispersed cases. A "fail safe" deployment will be performed at a navigated altitude of 6 km if the guidance deployment command has not occurred before then.

Derivation of influence coefficients

The goal of the ETPC guidance is to deliver the lander vehicle as nearly as possible to the desired parachute deployment target within an acceptable energy level to accomplish a successful landing. Because bank angle is the only guidance flight control effector, it is not possible to acquire and follow the nominal trajectory profile throughout the entry phase in the presence of dispersions. Instead, the guidance controls to a combination of perturbations in drag acceleration and radial velocity about the nominal profile, which will result in predicted final range convergence at terminal velocity arrival. This control law is referred to as "terminal point control using influence coefficients". In order to adequately predict the total range that will be flown from the current velocity to the terminal point velocity, the sensitivity of range to perturbations in drag acceleration and radial velocity must be determined. Since the control effector is vertical L/D, the influence coefficients of range with respect to L/D must also be determined.

The first step in the guidance configuration process is the design of an appropriate nominal entry reference trajectory profile. This is accomplished by shaping an open loop bank angle history to produce a trajectory that is consistent with the nominal entry interface delivery conditions, entry vehicle configuration, and Mars atmospheric environment, and provides adequate margins for dispersions. The in-plane equations of motion associated with atmospheric flight can be expressed in terms of four state variables as follows,

$$\frac{ds}{dt} = v\cos\gamma \tag{4}$$

$$\frac{dv}{dt} = -\left(\frac{D}{m} + g_S \sin\gamma\right) \tag{5}$$

$$\frac{d\gamma}{dt} = \frac{L\cos\phi}{mv} + \left(\frac{v}{r_e + h} - \frac{g_S}{v}\right)\cos\gamma \tag{6}$$

$$\frac{dh}{dt} = v\sin\gamma \tag{7}$$

where $s(t)$ is range, $v(t)$ is relative velocity, $\gamma(t)$ is the relative flight path angle, $h(t)$ is altitude, ϕ is the bank angle, m is the vehicle mass, r_e is the planet equatorial radius, and g_s is the gravitational acceleration at the surface. To determine the effects of small perturbations in the state variables and bank angle, these equations can be linearized about the nominal reference trajectory

$$\frac{d(\delta x)}{dt} = \left(\frac{\delta f}{\delta x}\right)_{x^*,u^*} \delta x(t) + \left(\frac{\delta f}{\partial u}\right)_{x^*,u^*} \delta u \tag{8}$$

where $x(t)$ is the vector of state variables, and $u = L \cos \phi$. Perturbations in the final range can be expressed as

$$\delta Rf = \lambda(t) \cdot \delta x(t) \tag{9}$$

where $\lambda(t)$ is a vector of influence coefficients which must satisfy the following system of differential equations that are adjoint to the linearized equations of motion.

$$\frac{d\lambda}{dt} = -\left(\frac{\delta f}{\delta x}\right)^T_{x^*,u^*} \lambda(t) \tag{10}$$

By selection of the appropriate boundary conditions at the final time and reverse integrating the adjoint differential equations along the nominal reference trajectory, the solution is found for $\lambda(t)$. This solution is then transformed to the velocity domain, and the final influence coefficients for the longitudinal control equations (1) and (2) are derived as follows.

$$\frac{\delta R}{\delta D} = F_1(v) = -\frac{m h_s^*(v)}{D^*(v)} \lambda h(v) \tag{11}$$

$$\frac{\delta R}{\delta \dot{r}} = F_2(v) = \frac{\lambda_\gamma(v)}{v \cos \gamma^*(v)} \tag{12}$$

$$\frac{\delta R}{\delta(L/D)} F_3(v) = \lambda u(v) \tag{13}$$

MONTE CARLO DISPERSIONS

The EDL sequence was statistically tested in a Monte Carlo analysis by varying parameters within several simulation models including the atmosphere, aerodynamic data, mass properties, control system, and navigation system. These dispersed quantities were varied using either a uniform or Gaussian distribution. Additional variables were added to simulate the variation in initial position and velocity due to variations in the interplanetary trajectory, and the spacecraft's initial attitude. These variations are called mission uncertainties.

The atmospheric dispersions model varies the density profiles that the spacecraft would encounter during EDL. The range of density profiles, shown in Figure 6, illustrates that the spacecraft must be designed to tolerate density variations that range from 80% lower than the mean to over 100% higher than the mean for high altitudes, and variations between 30% lower to 30% higher than the mean at parachute deployment.

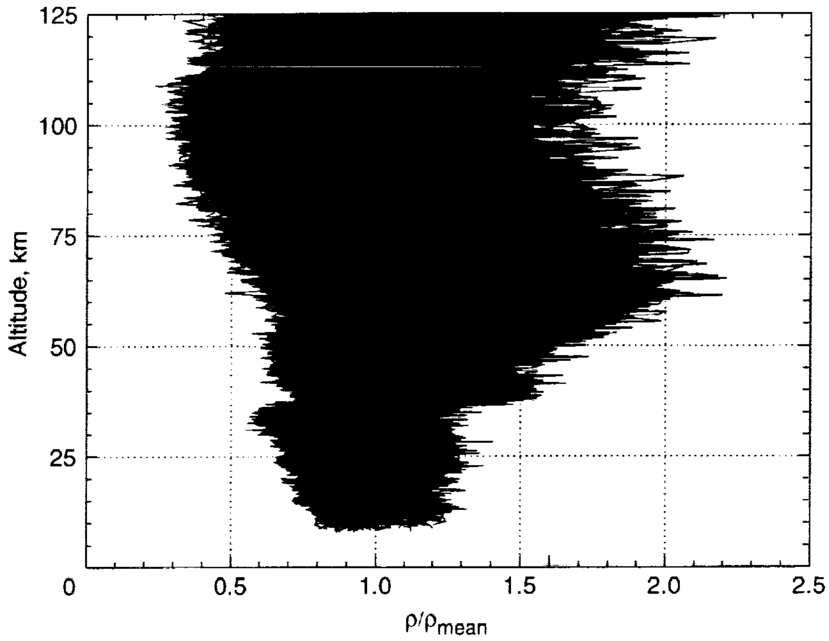

Figure 6 Mars Atmospheric Density Variation

Aerodynamic uncertainties are determined for the entry phase to cover the range of flow regimes of free molecular, transitional, and hypersonic to low supersonic continuum. Uncertainties were generated for each of these individual regions. Blending functions are used between these regions. The uncertainties were generated by the aerodynamic community and were based on flight experience with Viking, Mars Pathfinder, etc. The total aerodynamic uncertainties include a variation in axial and normal force coefficient, and a variation in the trim angle of attack of ±2° to simulate uncertainty in the pitching moment. Modeling uncertainties in axial and radial center of gravity generate another variation. Figure 7 shows the effect of these uncertainties on the L/D at Mach 3 and Mach 24. The total variability in L/D is ≈±25% with 6% due to the cg variation, 18% from the 2° angle of attack increment to account for trim variations, and only 1% from the aerodynamic normal force and axial force coefficient uncertainties.

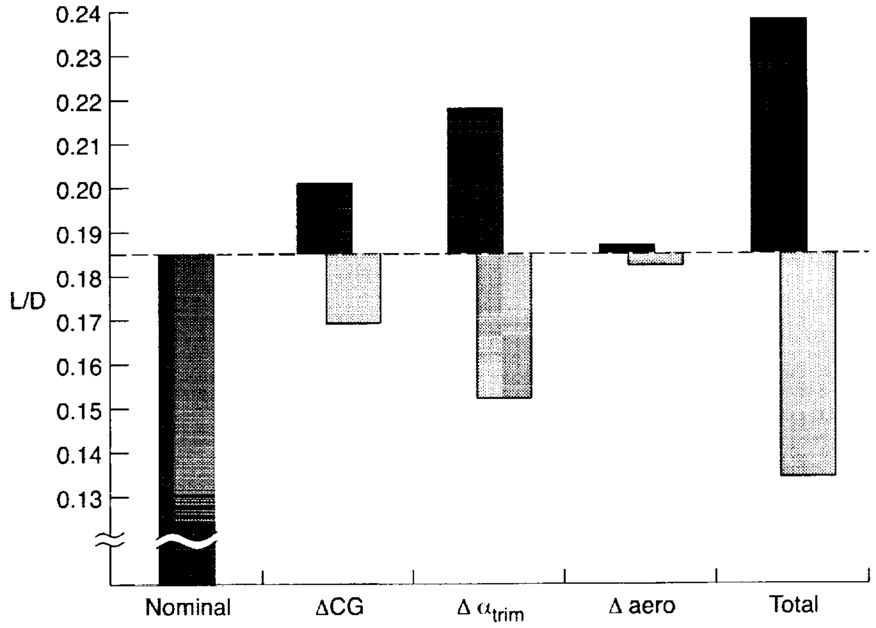

Figure 7a Contributions to L/D Uncertainties, Baseline Vehicle, Mach 3

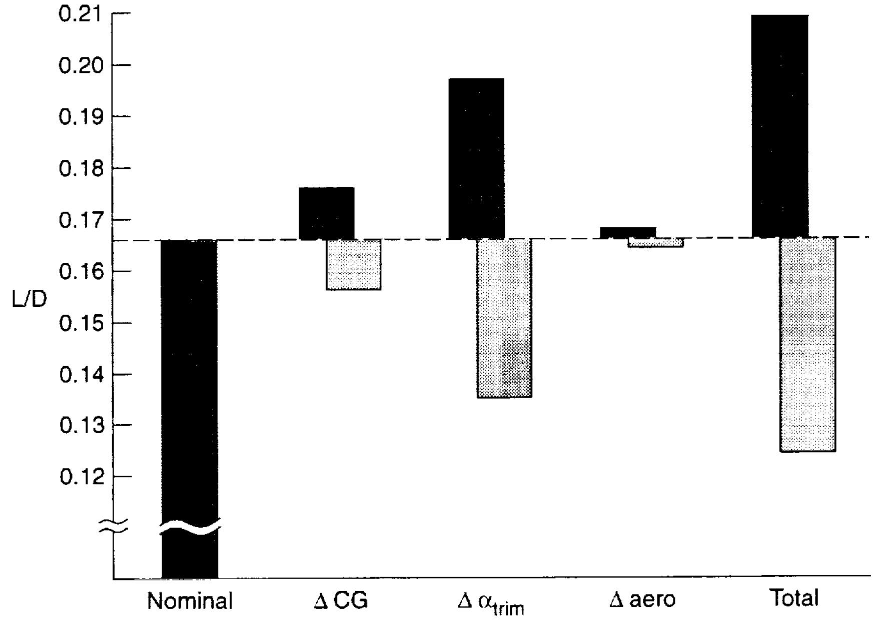

Figure 7b Contributions to L/D Uncertainties, Baseline Vehicle, Mach 24

The control system dispersions, for atmospheric interface to parachute deployment, are defined by the effectiveness of the reaction control system to provide bank angle acceleration. This acceleration was varied by ±10%.

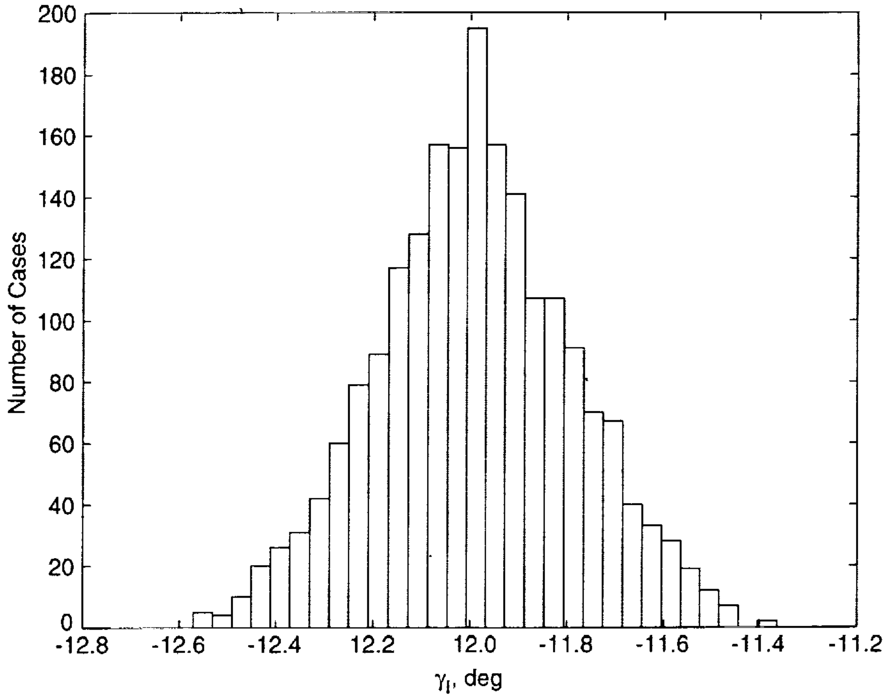

Figure 8a Distribution of Entry Flight Path Angle (Radiometric Navigation)

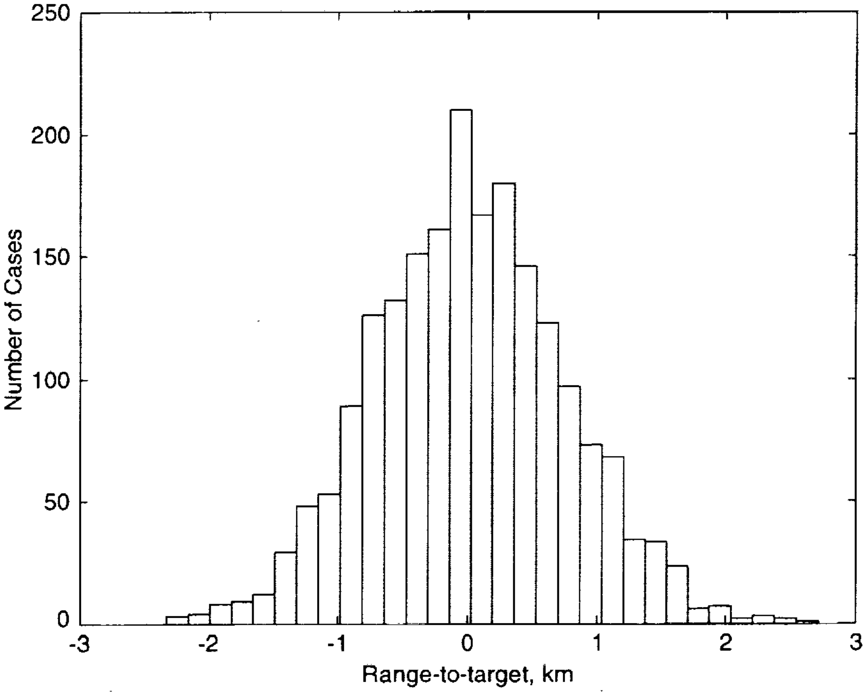

Figure 8b Distribution of Entry State Range From Nominal Variation (Radiometric Navigation)

The mission dispersions include actual delivered entry state, knowledge errors in that state, initial spacecraft attitude. For the baseline 2nd generation lander mission, only the availability of radiometric data is assumed. Radiometric means that the position and velocity of the spacecraft is derived only from Deep Space Network observations of the spacecraft. (The advantages of a technique that combines these measurements with optical observations of Deimos and Phobus by the spacecraft will be described later.) Figure 8 illustrates the range of uncertainties in the delivery states and the knowledge of those states. Figure 8a shows that the variation in the delivery flight path angle is ±0.6° around a nominal of 12°. Steeper flight path angles will, in general, require the spacecraft to fly a more lift-up than nominal trajectory compared to the nominal, and the shallower flight path angle will require a more lift-down trajectory than nominal. Figure 8b shows the knowledge horizontal error profile. The knowledge error is the difference in the actual parameter and the parameter, as it would be observed. The range of knowledge errors in horizontal range is ≈±2 km. The horizontal knowledge error, as will be shown later in this paper, is a major contributor to the final range errors. The guidance algorithm has no knowledge of this error and thus cannot correct it.

MONTE CARLO SIMULATION RESULTS

This paper focuses on the entry phase of EDL and results below will be presented at supersonic parachute deploy. The minimum altitude of the supersonic parachute deploy is defined such that a soft touchdown is achieved with the vehicle and mission dispersions. In addition, the footprints at parachute deploy are indicative of the footprints at touchdown, the primary additional factor that affect the footprints at touchdown are wind dispersions.

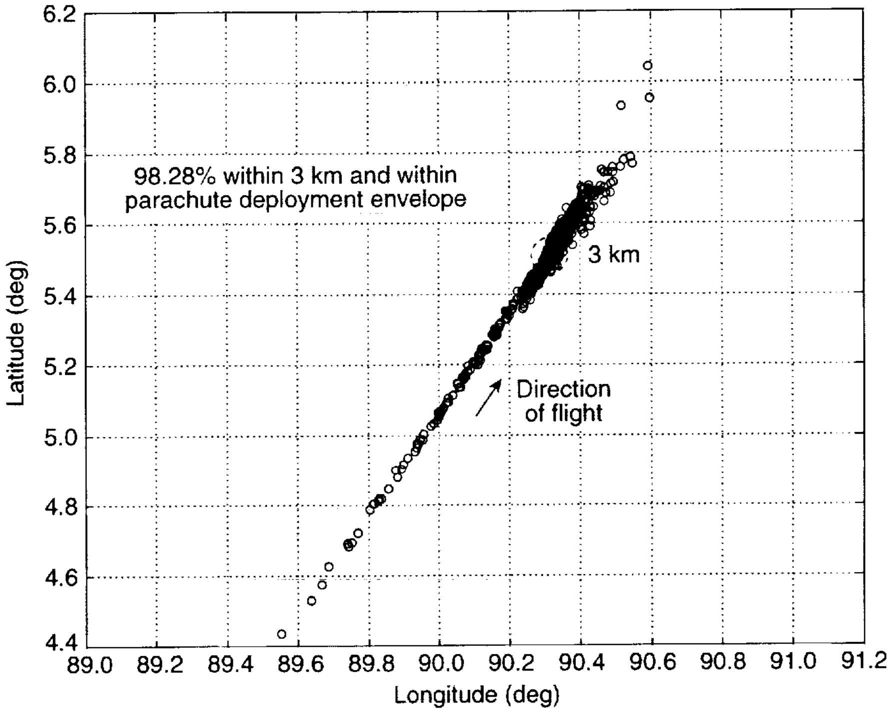

Figure 9a Monte Carlo Results for Supersonic Parachute Deployment Footprint (All Dispersions:- Radiometric Navigation)

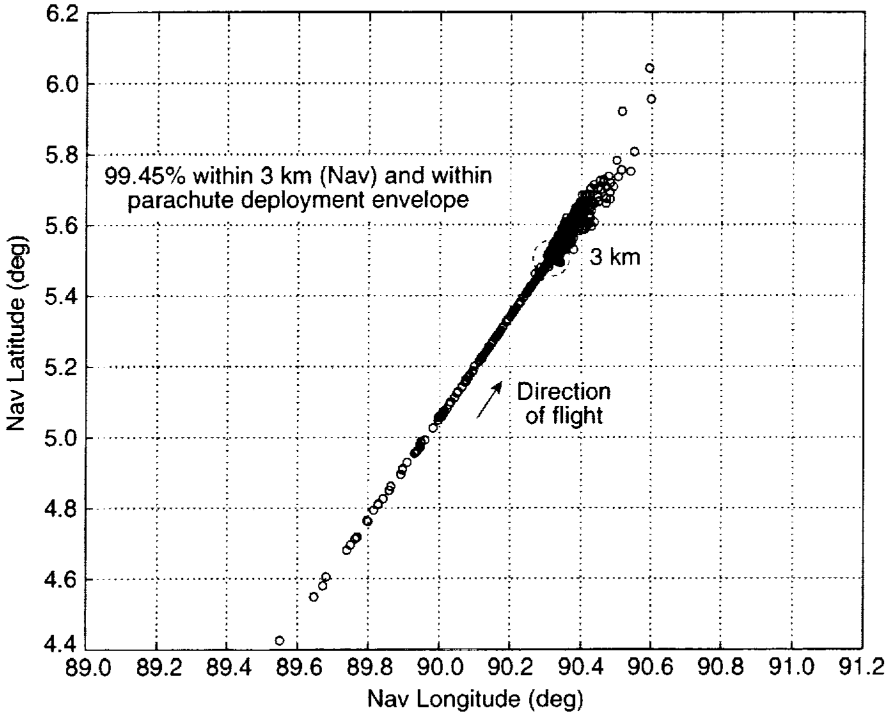

Figure 9b Monte Carlo Results for "Nav" Predicted Supersonic Parachute Deployment Footprint (All Dispersions:- Radiometric Navigation)

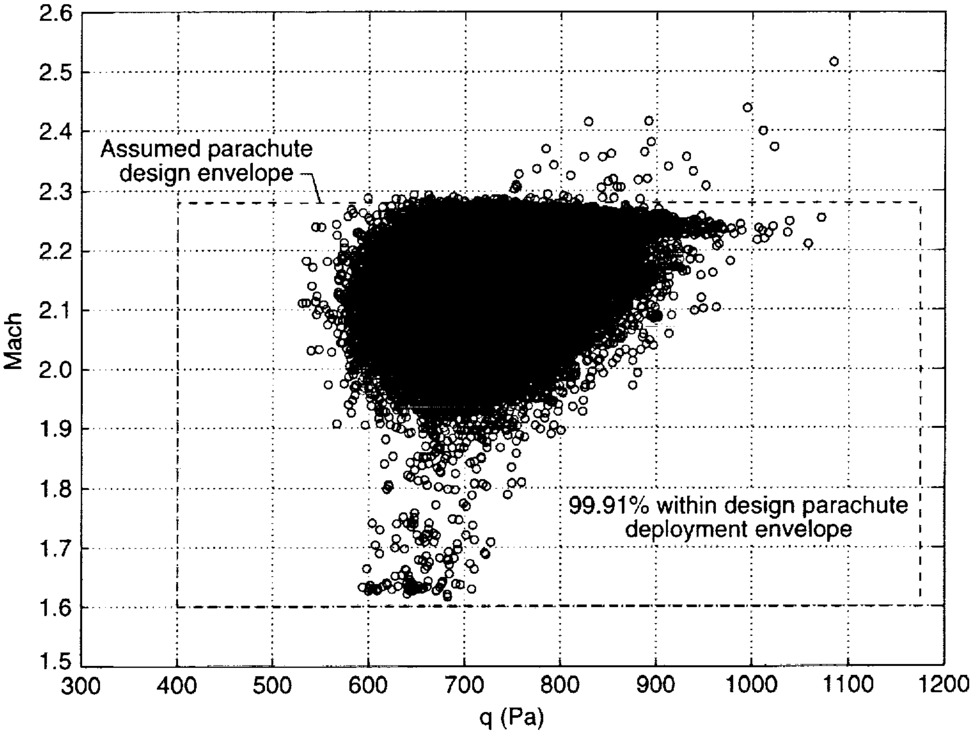

Figure 9c Monte Carlo Results for Supersonic Parachute Deployment Conditions (All Dispersions:- Radiometric Navigation)

Figure 9 shows the results of one hundred thousand simulations generated with a Monte Carlo analysis. These simulations include all of the uncertainties and deviations described above. As stated earlier, the goal of this design is to develop a spacecraft that is within 3 km of the target at landing, deploys within the supersonic parachute deployment envelope limits, and touches down safely at least 99.7% of the time. Figure 9a shows the range distribution at parachute deployment for the spacecraft and mission design assumptions described above. With this set of assumptions, the baseline demonstrated a success rate of 98.28%. Note that the guidance algorithm is designed to sacrifice range to provide a safe touchdown. This is accomplished by determining the minimum altitude for which supersonic parachute deployment can occur such that safe touchdown results at least 99.7% of the time. This altitude is implemented as a minimum altitude supersonic chute deploy override in the guidance algorithm. Examination of Figure 9b shows the "Nav" success rate to be 99.45%. Figure 9c shows the parachute deployment was within the design envelope 99.91% of the time – thus meeting the design criteria.

The major error sources in footprint and parachute deploy conditions were determined by running Monte Carlo simulations with isolated sets of related variables. These sets of related variables include: entry state position and velocity variation with and without knowledge errors, aerodynamics, and atmospheric density. The results, summarized in Table 2, reveal that no single factor is leading to the large maximum range error when all dispersions are considered ("Baseline"). The table shows that the largest contributor to range error is the combination of dispersed entry states including knowledge errors. The maximum range seen with aerodynamic and atmospheric uncertainties was within the design requirements. All of the above sets of dispersions contribute to the spread in dynamic pressure at parachute deployment. The atmospheric dispersions are largest contributor to the spread in Mach number at parachute deployment.

TABLE 2

INFLUENCES OF INDIVIDUAL MAJOR ERROR SOURCES

Case Description	Maximum Range Error, km	Parachute Deploy Dynamic Pressure Range Δ Pa	Parachute Deploy Mach Range,
Δ Mach			
Baseline	75	545	0.9
Entry States Dispersion Only	4.7	306	0.2
Entry States + Entry States Knowledge Dispersions Only	5.8	298	0.2
Aerodynamic Dispersions Only	0.3	231	0.1
Atmospheric Dispersions Only	1.2	203	0.4

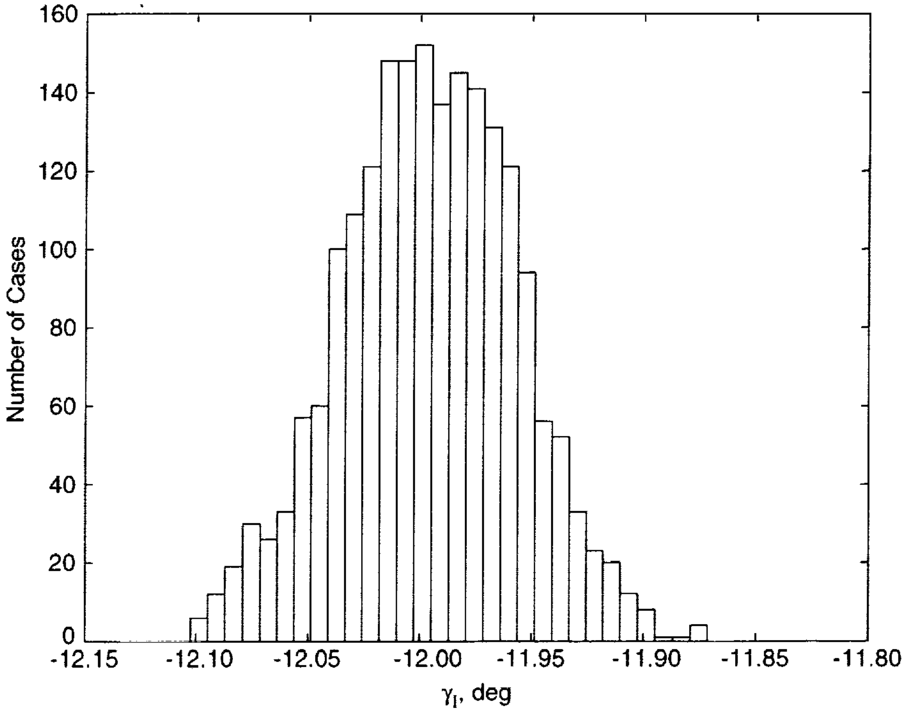

Figure 10a Distribution of Entry Flight Path Angle (Radiometric + Optical Navigation)

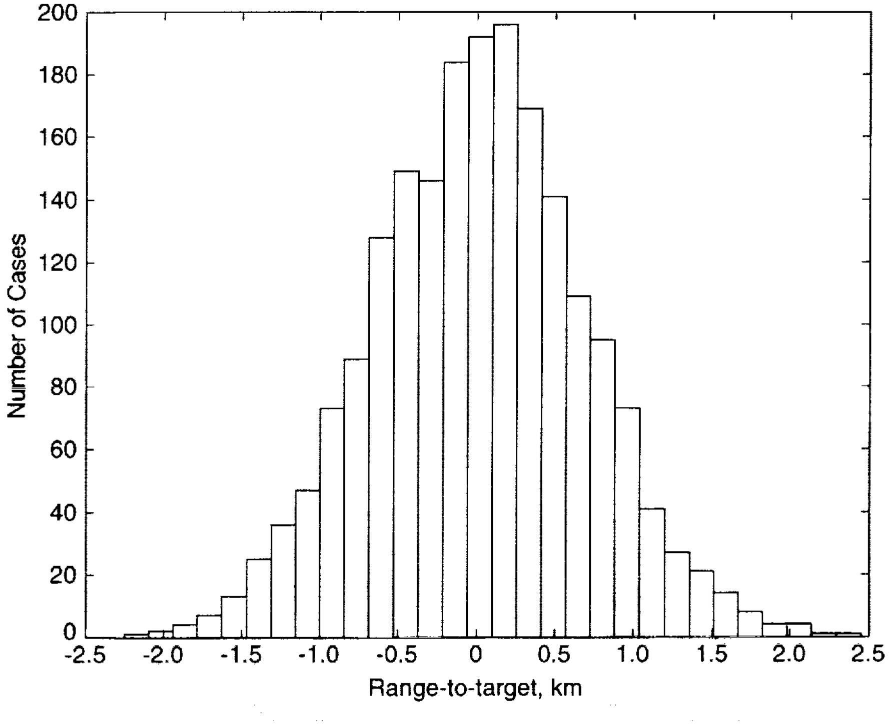

Figure 10b Distribution of Entry State Range From Nominal Variation (Radiometric + Optical Navigation)

The objectives for the vehicle and mission design are to meet the footprint, parachute deploy and touchdown criteria with radiometric navigation only. As will be discussed, beginning in the section "Vehicle Parameters for Effective Aeromaneuvering" below, modifications to the vehicle are necessary, and in progress, to meet these objectives. System robustness can be increased however with the addition of optical navigation technology. Optical navigation reduces the errors at atmospheric interface, which reduces the dispersions that the guidance must correct. An initial estimate of the radiometric plus optical navigation states, shown in Figure 10, have been implemented in the simulation to quantify the benefit from this technology. Comparing Figures 8 and 10, the dispersion in flight path angle has been reduced from ≈±0.6° for the radiometric navigation only to ≈0.1° for the radiometric plus optical navigation. The horizontal range error for the radiometric plus optical navigation remained the same as for the radiometric only cases.

Figure 11 shows the simulation results using all dispersions and optical navigation. With this change the success rate has increased from 98.28% to 99.58%, with the "Nav" predicted success increasing from 99.45% to 99.98%. This improvement in navigation accuracy has provided a significant increase in success, but still falls just short of the goal. Another observation is that the extreme range cases have also been eliminated. For the radiometric cases, the largest range error was ≈75 km, where the largest range error for the radiometric with optical is ≈6 km. This increased success rate and large reduction in extreme range cases is due to the reduction in initial flight path angle variability.

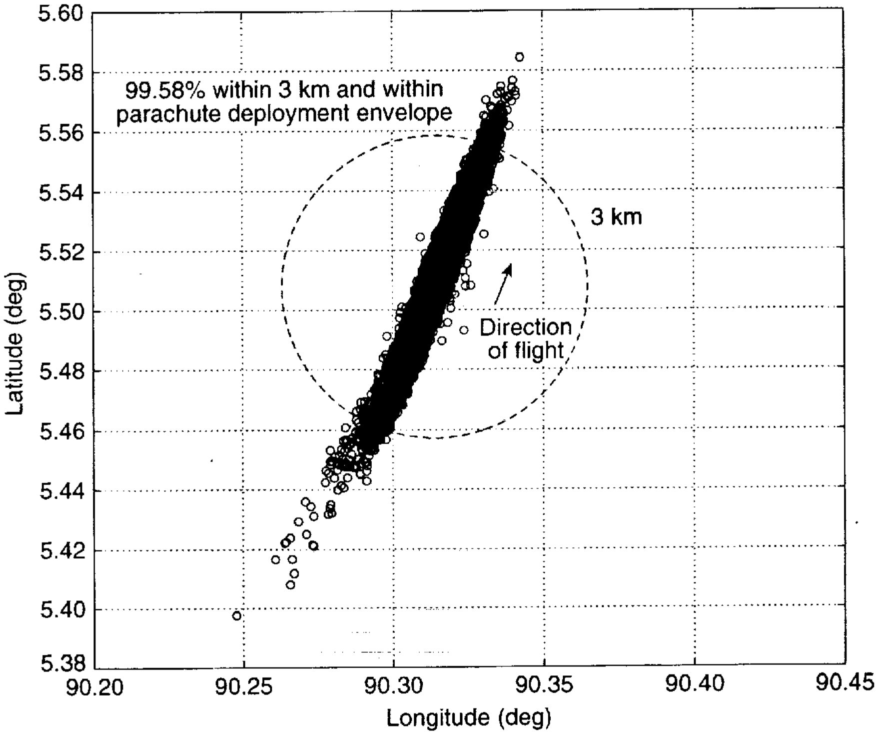

Figure 11a Monte Carlo Results for Supersonic Parachute Deployment Footprint (All Dispersions:- Radiometric + Optical Navigation)

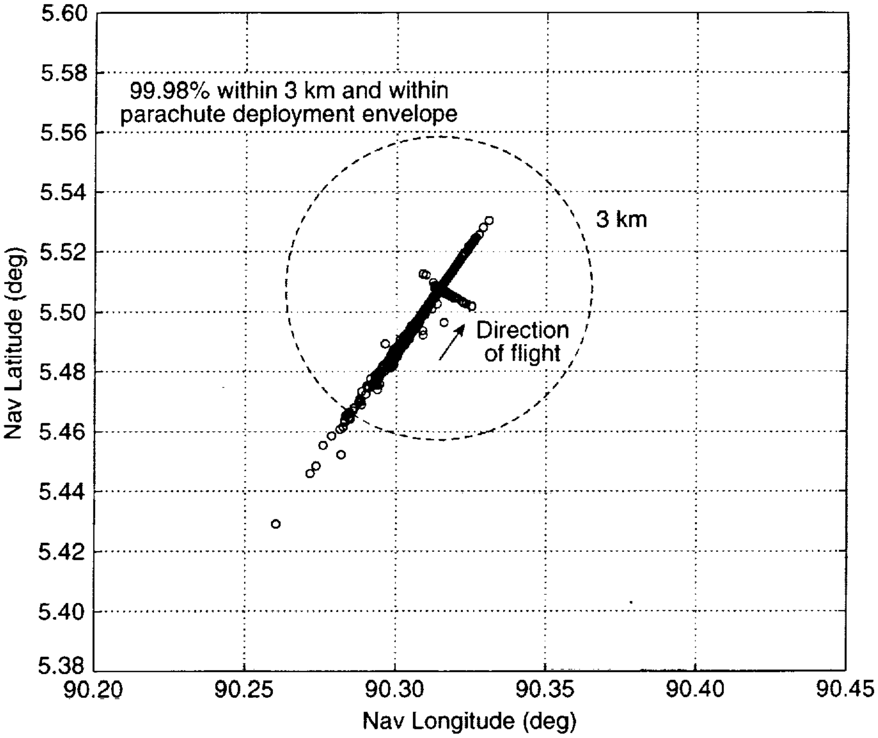

Figure 11b Monte Carlo Results for "Nav" Predicted Supersonic Parachute Deployment Footprint (All Dispersions:- Radiometric + Optical Navigation)

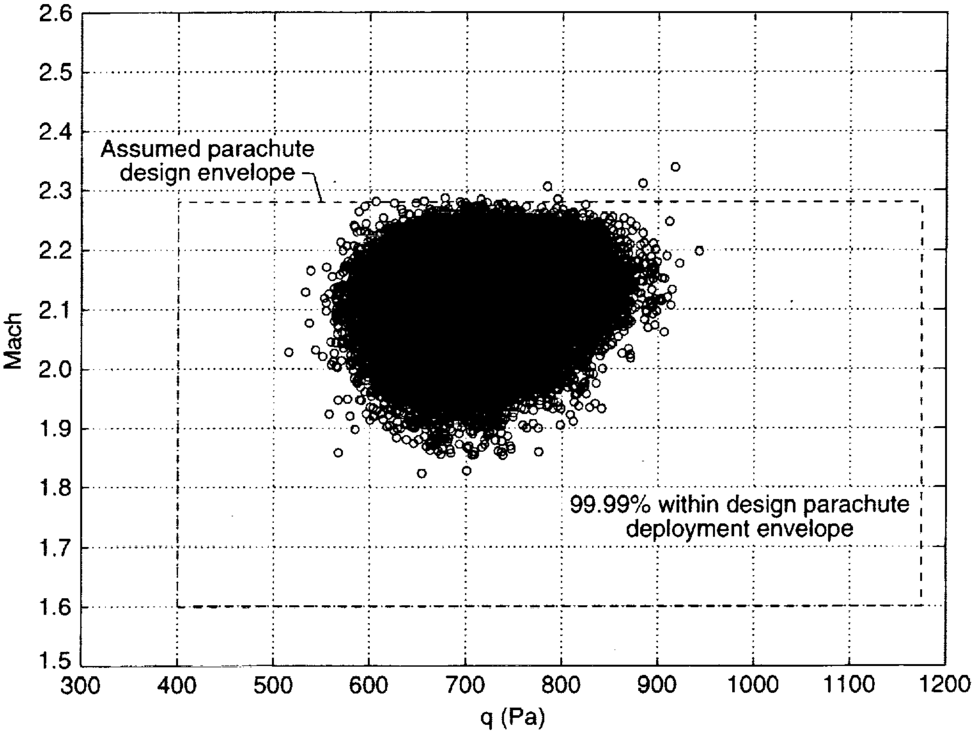

Figure 11c Monte Carlo Results for Supersonic Parachute Deployment Conditions (All Dispersions:- Radiometric + Optical Navigation)

VEHICLE DESIGN PARAMETERS FOR EFFECTIVE AERO-MANEUVERING

To achieve a precision landing in the presence of dispersions, aeromaneuvering must be employed during the hypersonic entry region to converge the range errors caused by delivery state errors and variations in atmospheric density and vehicle aerodynamic characteristics. The entry guidance receives the knowledge state as an input from the navigation system, and provides bank angle commands to steer the trajectory to the desired terminal point conditions at parachute deployment. To successfully accomplish this task, the vehicle must be designed to provide sufficient control authority.

The planar equations of motion for atmospheric flight can be expressed as

$$\frac{dV}{dt} = -\left(\frac{\rho g^2}{2\beta_m}\right)V^2 - g\sin(\gamma) \tag{14}$$

$$V\frac{d\gamma}{dt} = \left(\frac{\rho g^2}{2\beta_m}\right)V^2\left(\frac{C_L}{C_D}\right)_V - \cos(\gamma)\left[g - \frac{V^2}{R_e + h}\right] \tag{15}$$

where ρ is atmospheric density, γ is flight path angle, and β_m is the vehicle ballistic coefficient. This ballistic coefficient is defined as the mass cross sectional density of the vehicle divided by the drag coefficient.

$$\beta_m = \frac{m}{C_D S} \tag{16}$$

Lift-to-drag ratio (L/D)

The primary contributor to entry range dispersion is the delivery error in the flight path angle at entry interface. An error in the initial flight path angle results in a diverging range error with respect to the nominal reference trajectory profile. This range error will continue to increase until sufficient atmospheric density has been encountered to provide effective flight path angle control. Targeting for a steeper nominal entry flight path angle will result in smaller range errors, but will also result in larger vehicle load factors and less available flight time to converge the range errors. For the Mars 2005 direct entry conditions, it has been found that a flight path angle of approximately –12 deg to –13 deg provides the best compromise between these effects. As can be seen in equation (15), the rate of change of flight path angle is directly proportional to the in-plane vertical component of L/D. The magnitude of the L/D required to achieve the target range is a function of the delivery error and the amount of flight time remaining, as well as the variations in vehicle L/D and atmospheric density. For a given worst-on-worst combination of the above dispersions, the vehicle trimmed lift coefficient may be scaled to determine the minimum required L/D which will provide sufficient control authority to achieve the target. For the 2nd generation lander in the 2005 opportunity, it has been determined that a minimum nominal average L/D of 0.22-.25 is required to successfully achieve the desired terminal range in the presence of the 0.6 deg delivery flight path angle errors resulting from radiometric-only navigation. Maximum range errors of approximately 110 km must be converged in these cases.

Ballistic coefficient

A vehicle design that provides an adequate L/D for trajectory range control will not necessarily achieve acceptable terminal conditions if the ballistic coefficient is not compatible with the parachute deployment constraints. As can be seen in equation (14), the deceleration due to drag is larger for smaller ballistic coefficients. The atmospheric density required at terminal entry conditions to achieve a given velocity and drag acceleration at parachute deployment will increase in direct proportion to the ballistic coefficient. Therefore, either the parachute deployment speed (Mach number) must increase and/or the deployment altitude must decrease for vehicles with larger ballistic coefficients.

The parachutes currently in use by the Mars robotic lander program were certified to a deployment envelope based on the Viking lander design, which had a ballistic coefficient of approximately 75 kg/m^2. The Mars Pathfinder and MSP '01 lander designs had similar ballistic coefficients to Viking, and were capable of achieving the required parachute deployment Mach number and dynamic pressure envelope at nominal altitudes of approximately 15 to 16 km. The baseline configuration has a ballistic coefficient of approximately 114 kg/m^2 at parachute deployment. To maintain the deployment Mach number within the Viking envelope, the nominal altitude at deployment must necessarily decrease by 30%, to approximately 10.5 km. Dispersions in drag coefficient and atmospheric density result in a large variation in the deployment altitude as shown in Figure 12. To preserve adequate time to accomplish a safe terminal deceleration and landing to a 2.5 km elevation site, a backup deployment command is issued at a minimum navigation calculated altitude of 6 km. Many cases were triggered by this backup deployment command. Therefore, with ballistic coefficients any larger than the baseline, the range accuracy at deployment will degrade as a result of having no remaining margin from the parachute deployment constraints.

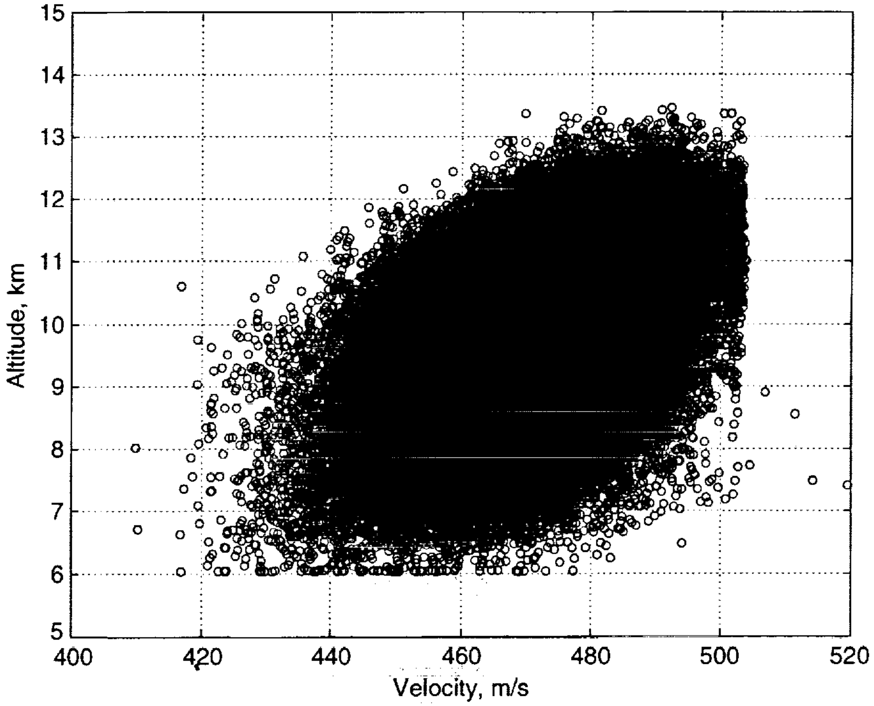

Figure 12 Monte Carlo Results for Supersonic Parachute Deployment Conditions (All Dispersions:- Radiometric Navigation)

CONFIGURATION DESIGN FOR A 2ND GENERATION LANDER

Design of the 2nd generation lander outer moldline (OML) will be described in this section. Figure 13 shows the initial baseline configuration and a representative set of candidate configurations considered in the design trade. The capsule configuration was selected for the baseline because it provides a low ballistic coefficient for a given vehicle mass, it meets the original low L/D requirement of .18, and has significant flight heritage. In addition the payload volume requirements for the lander fit within the capacity available for capsules packaged in existing launch vehicle fairings. Capsule configurations were continued in the design trade due to the reasons described above and because of the expected ability of the configuration to meet the L/D requirements of .22-.25.

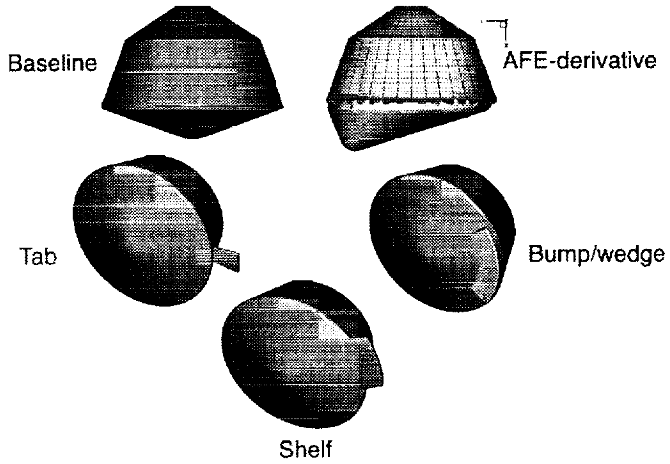

Figure 13 Configuration Classes

In addition to the L/D (0.22-0.25) and M/C_DS (<120 kg/m^2) requirements the aeroshell configuration must be developed to meet several additional objectives and requirements. The vehicle must fit in the max static payload diameter for the Atlas V launch vehicle with a 5m payload shroud. The baseline concept load path at launch, as shown in Figure 2, must be maintained. In addition, the mass required to achieve the L/D must be minimized. It is also desirable to minimize the sensitivity of the L/D and M/C_DS to axial cg location. This minimizes the sensitivity of the aeroshell design to packaging through the design evolution and also minimizes the impact of mass uncertainties on flight performance for the final design. Throughout the conceptual design, the backshell was assumed to remain the same as the baseline, and it was desirable to minimize changes to the internal packaging.

The baseline concept achieves the L/D by utilizing ballast to provide a radial cg offset, such that the vehicle trims at an angle of attack. The required radial cg offset, angle of attack, L/D, and M/C_DS for the baseline are shown in Figure 14. (Axial force is the primary contributor to the lift vector, thus flying at a negative angle of attack produces a positive lift.) In the continuum regime, the L/D varies from ~.165 to ~.19, as shown in Figure 15a, from hypersonic Mach numbers to parachute deploy, respectively. Over the same Mach number range, the M/C_DS varies from 112 to 117 kg/m2, as shown in Figure 15b. To achieve the L/D =.25, the radial cg offset must be increased to achieve trim at a higher magnitude of angle of attack. Figure 14 shows the variation in trim angle of attack, L/D and M/C_DS with radial cg offset. As expected, an increase in L/D also produces an increase in the ballistic coefficient. However, the M/C_DS remains within the constraints set above. Therefore the offset cg approach does result in a configuration that meets the L/D, M/C_DS, as well as the other constraints required to achieve the footprint requirements for radiometric navigation only. However, the ballast required to achieve the radial cg offset is not insignificant. Therefore the objective for the alternate configurations was to achieve performance similar or better than the baseline with the increased radial cg offset, but at a significantly lower mass penalty.

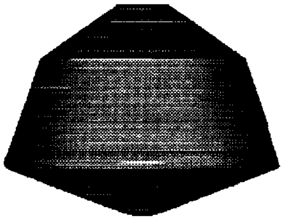

	Baseline	Baseline with Increased Radial cg offsets	
Alpha trim (°)	-11	-13	-15
CG rad/ max. vehicle diam	0.013	0.019	0.024
L/D	0.17**	0.21**	0.24**
M/CDA (kg/m^2)	112	117	121

Figure 14 Baseline configuration and baseline with increased radial cg offsets

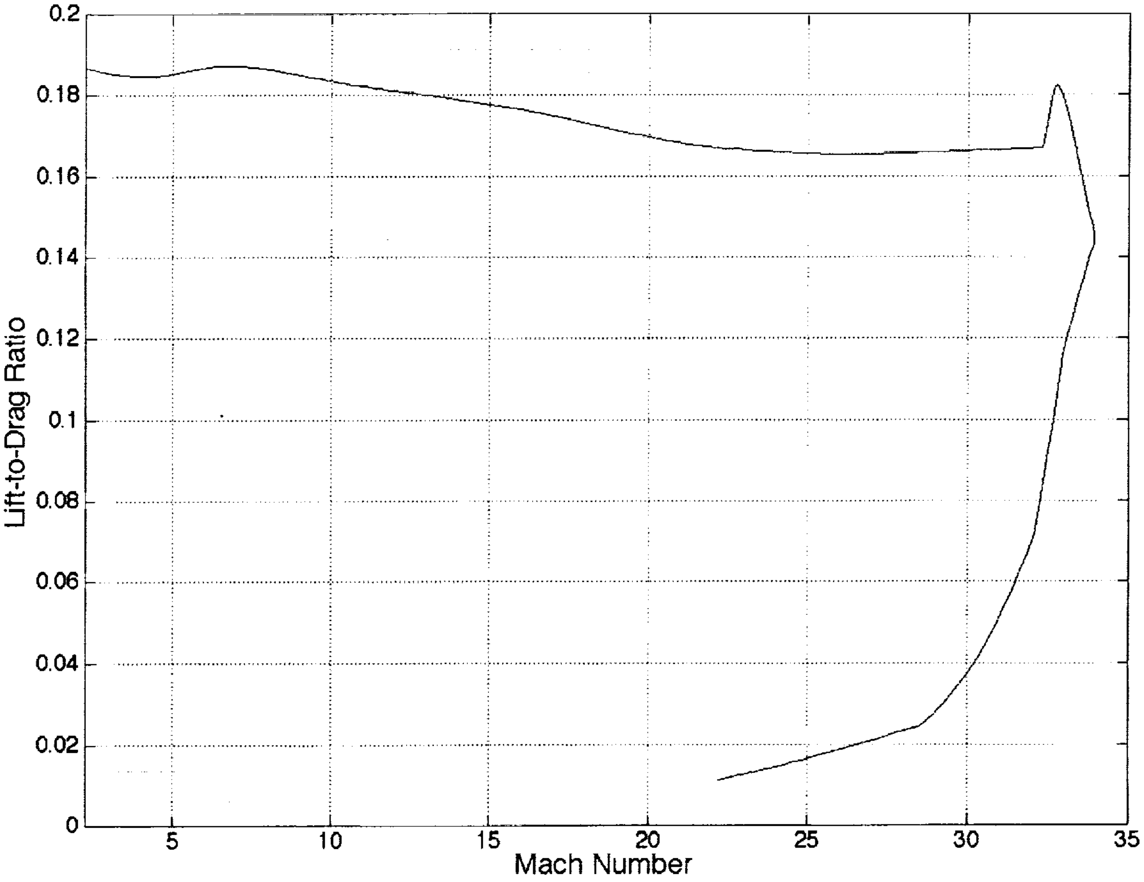

Figure 15a Baseline vehicle L/D vs. Mach along nominal trajectory

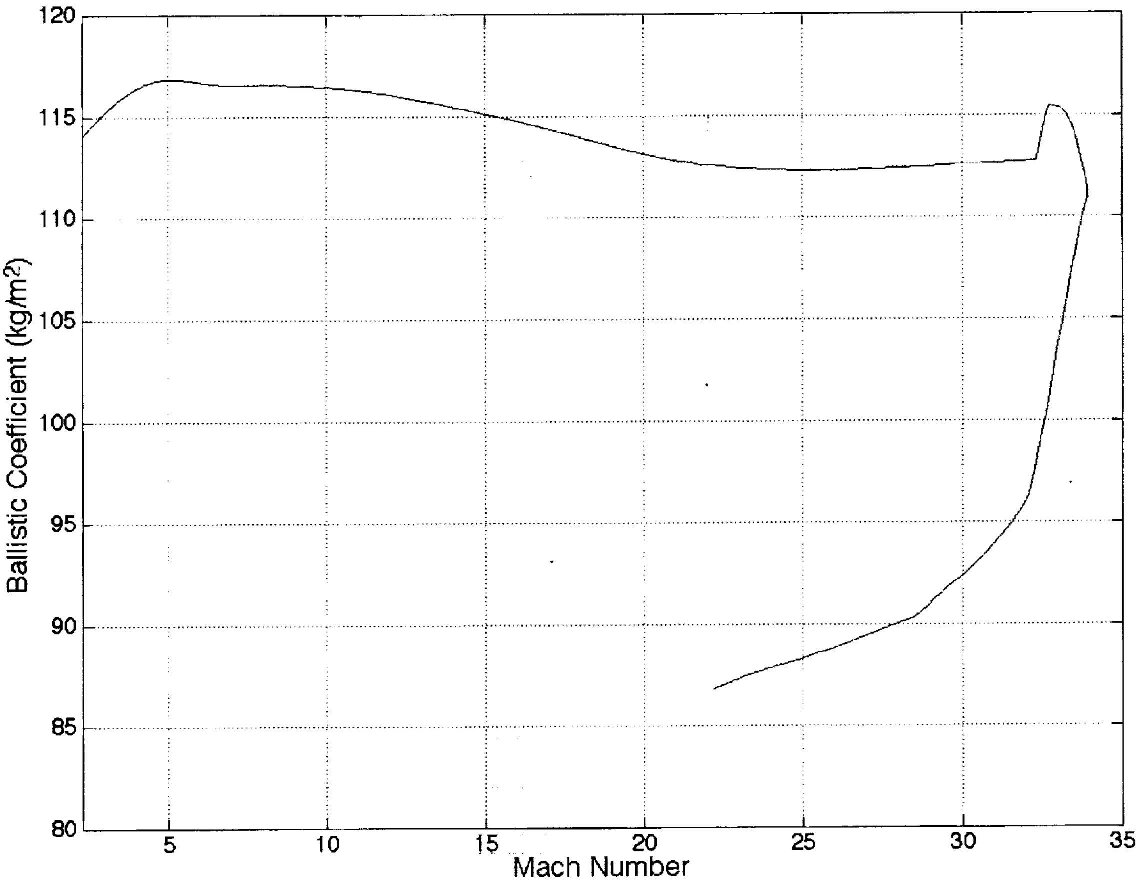

Figure 15b Baseline vehicle ballistic coefficient vs. Mach along nominal trajectory.

The next set of configurations explored were derivatives to the AFE geometry. Implementing the AFE geometry on the smart lander, the AFE smart lander configuration would achieve an L/D =.25, with an axial cg location ~45% farther forward referenced to the baseline nose and a radial cg offset of .028 referenced to the max vehicle diameter at an angle of attack of −15 deg. The objective was to modify the AFE shape to allow a similar level of performance as the original AFE, but with the axial cg located at the smart lander location and a zero radial cg offset. A parameterization of the AFE-derivative geometry is shown in Figure 16. Hypersonic aero performance was estimated using Newtonian analysis, and verified with CFD, for a range of configurations defined by the cone angle and rake angle. Through the analysis, the cg was assumed to remain at a constant axial station relative to the baseline nose location. This assumes that the axial cg location is governed primarily by the payload and backshell. The resulting L/D vs C_D plot as a function of cone and rake angles are shown in Figure 16. Shown on this same figure are the hypersonic values of C_D and L/D for the baseline, and the baseline with additional radial cg offsets to meet the increased L/D requirements. From this plot it is evident that this design space does not include an AFE-derivative configuration that meets the L/D =.25 and the $M/C_DS<$ 120kg/m2 requirement with zero radial cg offset, as highlighted by configurations 2,3*,4* and 5. The AFE-derivative 3* was tested in the 3-DOF simulation, and the guidance tuned to optimize the configuration performance. The 3* performance was only minimally better than that of the baseline, although the 3* requires no radial cg offset and trims at a lower angle of attack (beneficial to backshell heating).

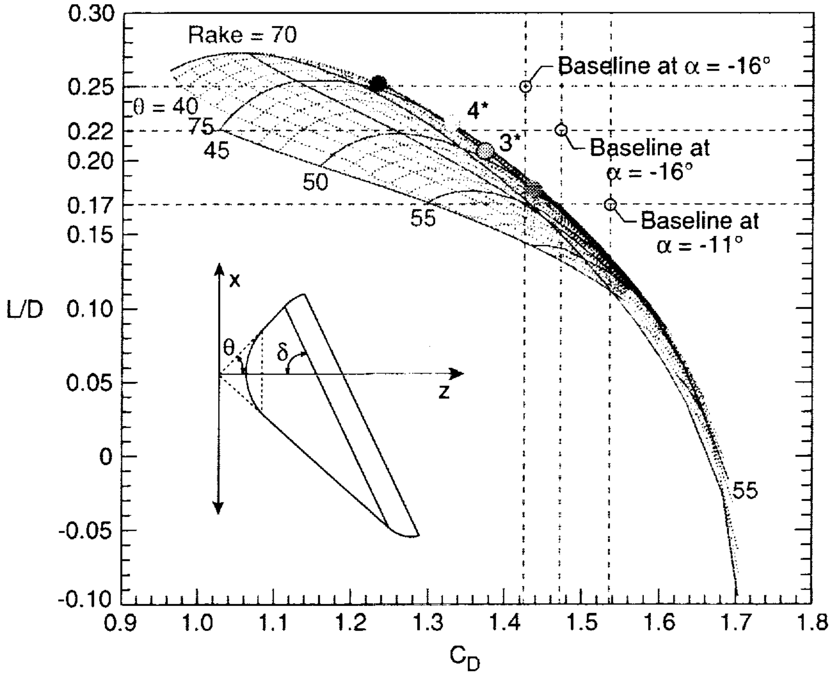

Figure 16 AFE-derivative geometry and aerodynamic performance at smart lander cg location.

Two additional shortfalls were identified for the AFE-derivative class of vehicles for application to a smart lander. As described previously, the baseline vehicle utilizes a cruise stage attached to the heatshield to carry the launch loads from the cruise stage through the heatshield and into the lander. With a heatshield shape that varies in axial distance from the lander pallet at the attachment points, the structure required to carry the launch loads through the heatshield to the lander are expected to result in a significant mass penalty, in addition to the increased complexity of the interface. In addition, the AFE-derivative configurations have a high sensitivity to axial cg location. Figure 17 shows a significant decrease in the L/D for each of the 2,3*,4* and 5 configurations for a cg 29% farther aft, referenced to the baseline nose, a possible location as the smart lander configuration evolves. With this aft location the design space does not include a configuration with an L/D as high as the baseline vehicle L/D. As a result in the configuration development, tight constraints would have to be placed on the axial cg location to eliminate the need to either modify the configuration through the design evolution, having significant impact on many of the subsystems and system performance, or end up with insufficient performance. While restrictions in axial cg movement are common constraints, the additional constraint resulting from the heatshield shape may be an unnecessary added complexity. Based on the above results, the AFE-derivative-class of configurations was eliminated for further consideration for the smart lander development.

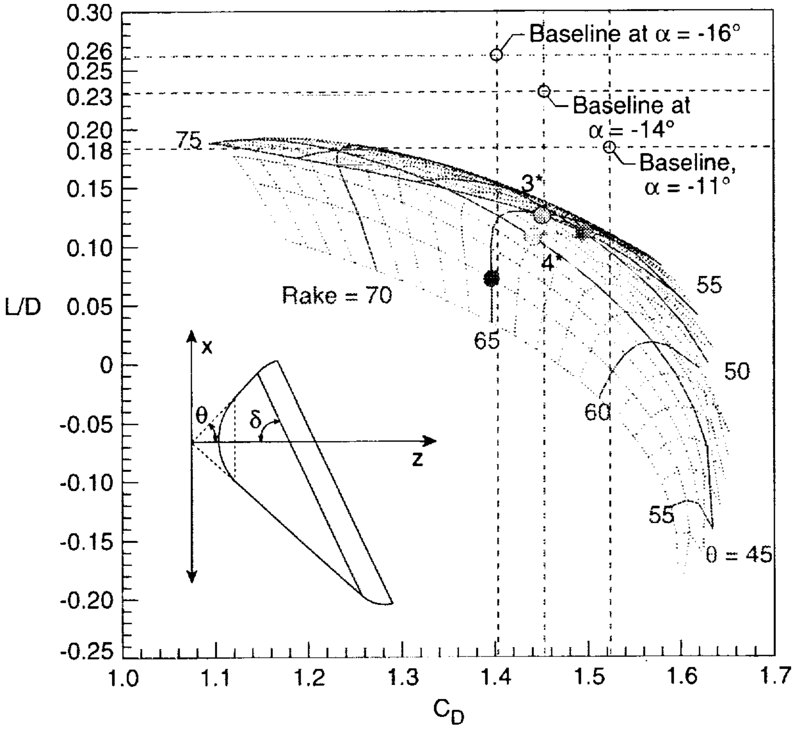

Figure 17 AFE-derivative design space with aft cg

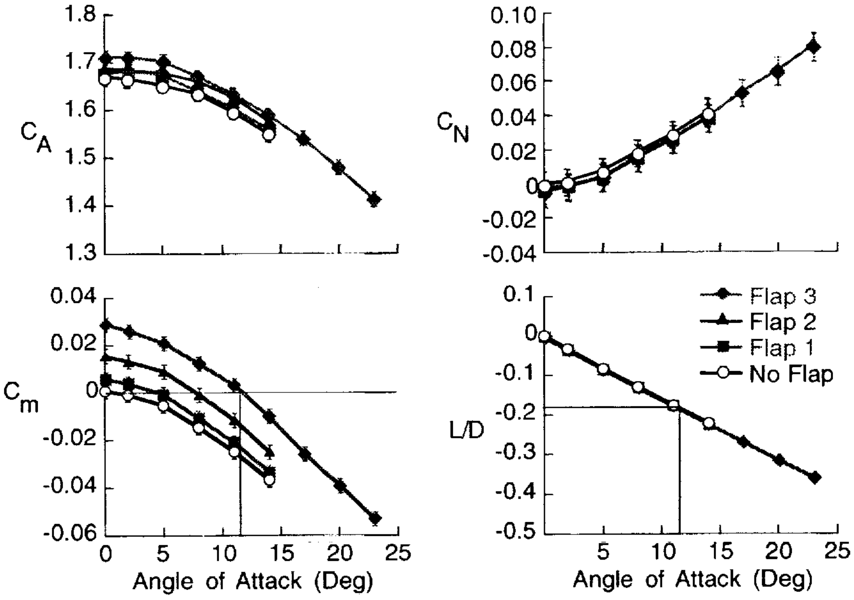

Figure 18 Effect of tab on aerodynamic coefficients. MSP '01 precision lander longitudinal aerodynamics LaRC Mach 6 CF4 tunnel.

Tab, shelf, and bump concepts, shown in Figure 13, were the other class of configurations investigated for application to the smart lander. Tab concepts were investigated as early as 1961 as reported in Reference 9, and considered again for the cancelled Mars Surveyor 2001 Precision Lander mission. The '01

Lander mission proposed utilizing a single time deployable tab to achieve the desired L/D for aeromaneuvering. The tab, similar to that shown in Figure 13, is angled 90 deg to the axis of symmetry of the 70 deg sphere cone heatshield and mounted behind the max diameter of the vehicle. This tab concept was tested in the LaRC M6 CF4 tunnel for aerodynamic force and moment coefficients for a range of tab sizes. As shown in Fig 18, the primary effect of the tab on the aerodynamics is to change the trim angle of attack of the vehicle. Otherwise the tab configuration has very similar aerodynamic performance to the baseline axisymmetric vehicle. In other words the tab is essentially the aerodynamic equivalent of a radial cg offset.

Building from the existing set of data available for the tab concepts, variations of the tab, shelf and bump concepts represented in Figure 13, were designed utilizing engineering estimates for aerodynamic performance to target an L/D =.25. Concepts were then analyzed with FELISA[10] Euler CFD at a given hypersonic Mach number over a range of angle of attack. Based on the CFD results, the configuration was either modified to achieve the target trimmed L/D or eliminated from consideration due to strong shock interactions, large nonlinearities in C_{m_α}, or inadequate performance potential. Configurations were also screened for M/C_DS and the sensitivity of L/D to axial cg location, d(L/D)/d(xcg). Variations of the tab and shelf concepts showed the most promise from this set of configurations. Figure 19 shows the coefficient of pressure at Mach 24, alpha=-15 deg for a configuration with an 80deg canted tab. The 80deg canted tab is located at the maximum diameter of the vehicle and is angled at 80degrees to the axis of symmetry of the 70deg sphere cone heatshield. This configuration trims at alpha=-16 deg with an L/D=25 and an M/C_DS = 114 kg/m2 at Mach 24.

Figure 19 Coefficient of pressure contours on canted tab at Mach 24 and –15deg angle of attack.

In general, the tab and shelf configurations have similar M/C_DS as the baseline configuration at -16deg angle of attack. They also have similar low variability of L/D with axial cg location. The tab and shelf concepts can each be sized to achieve the required L/D. The advantage of the tab concepts compared to the shelf concepts are that the tabs can be smaller, due to the higher pressure produced on the tab. A comparison of the baseline, baseline with additional radial cg offset, AFE-derivative 3*, canted tab and shelf concepts are summarized in Figure 20.

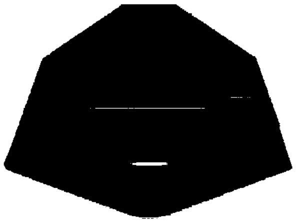

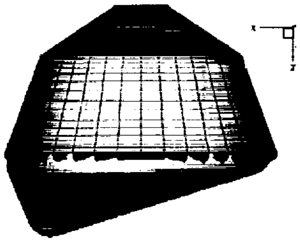

		Baseline		3* AFE-deriv
Alpha trim (º)	11	13	15	5.1
CG rad/max vehicle diam	.013	.019	.024	0
L/D	.17**	.21**	.24**	.21
M/CDA (kg/m ^{2})	112	117	121	129
d(L/D)/d(CG axial) (m $^{-1}$)	.045	.052	.056	-.37
d(L/D)/d(CG rad) (m $^{-1}$)	2.2	1.8	1.6	2.5
Issues:		**Mass**, Aft body heating		**Cruise ring interface, load** paths – mass. **Axial cg sensitivity.** **M/CDA increase w/L/D increase.**

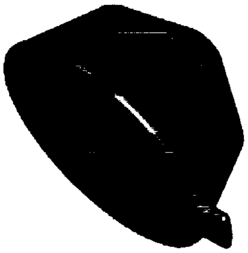

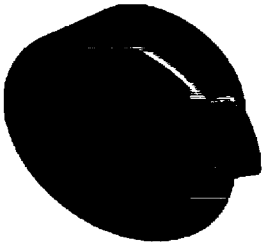

	Canted Tab	Shelf 2
Alpha trim (º)	-16	-14.2
CG rad/max vehicle diam	0	0
L/D	.25	.24
M/CDA (kg/m ^{2})	114	113
d(L/D)/d(CG axial) (m $^{-1}$	.050	.030
d(L/D)/d(CG rad) (m $^{-1}$	2.1	1.7
Tab area/Sref (%)	3.8	6.2
Issues (both):	Supersonic L/D, aft body heating, packaging, **tab heating, thermal**	

Figure 20 Configuration summary. Results reported at Mach 24 trim angle of attack.

The next screening step was to assess the aeroheating environments. Since the objective of the aeroheating screening was for feasibility, variations of the the tab geometry were selected for screening due to the expected higher levels of aeroheating and the more complex flowfields compared to the shelf concepts. The LaRC Mach 6 CF4 tunnel and the phosphor thermography approach[11] were selected. The peak heating point on the nominal 2005 smart lander trajectory (Mach 24) is more closely approximated by the Mach 6 CF4 tunnel compared to a Mach 6 air tunnel, due to the ratio of specific heats. The CF4 tunnel simulates approximately Mach 12 flow along the '05 smart lander trajectory. The thermographic phosphor approach allows global heating environments to be determined as a function of geometry and angle of attack relatively quickly. The objective of the test was to assess the relative merit and feasibility of one tab design relative to another and indicate future direction of the configuration development. In addition, this data is used for comparison to CFD. The heatshield, shoulder and backshell heating environments were also measured in the test.

The aeroheating environments from the test allowed for downselection to the canted tab from the tab class of concepts. Figure 21 shows the schleiren of the canted tab configuration, at −16 deg angle of attack, approximately at the hypersonic trim point, and shows the global tab and heatshield heat transfer coefficients normalized to the stagnation point. Note that the heating on the tab reaches nearly two times that of the vehicle stagnation point. Figure 22 shows the aeroheating on the backshell as a function of angle of attack. Note the increase in aeroheating with angle of attack. This data will be utilized with CFD to provide an initial estimate of the heating environments required to select and size the TPS system.

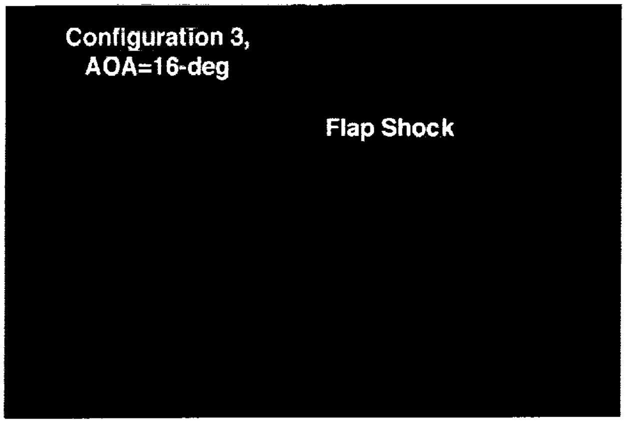

Figure 21a Schleiren of canted tab configuration in LaRC CF4 tunnel at alpha=-16deg

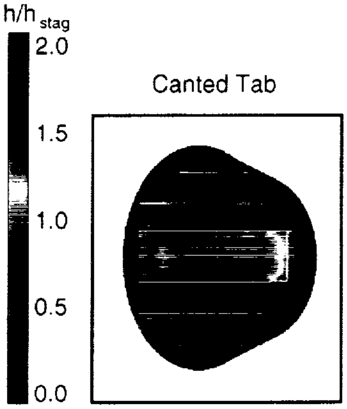

Figure 21b Heat transfer coefficient distribution on canted tab configuration from Phosphor Thermography measurements in LaRC CF4 tunnel at alpha = -16deg

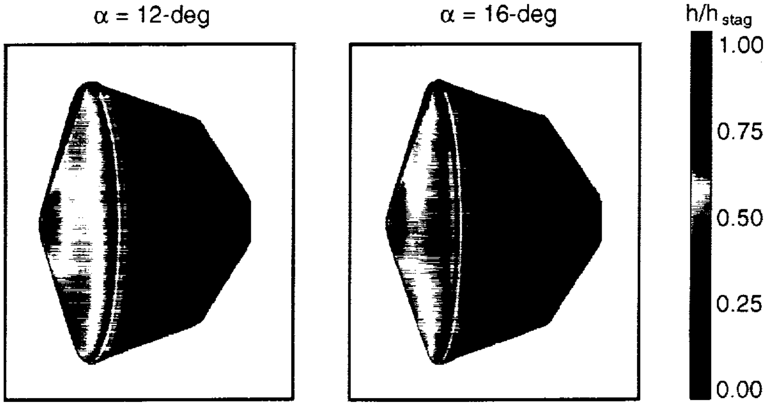

Figure 22 Windward side heating as a function of angle of attack. Heat transfer coefficients from phosphor thermography measurements in LaRC CF4 tunnel

After the aerodynamic and aeroheating screening, two classes of configurations have been selected for further development, the canted tab and the shelf concepts. Configurations are in the process of being modified based on aerodynamic, aeroheating, structure and TPS sizing analysis. Updates in mass estimates for the tab and shelf concepts will continue as structure and TPS design and selection progress. Concepts will be evaluated with the simulation and the guidance algorithm tuned for the specific configurations to determine their ability to meet the footprint, parachute qualification box and soft touchdown objectives. In addition, configurations will be tested in the LaRC Unitary tunnel for supersonic static aerodynamic coefficients, and tested in the ARC ballistic range primarily for dynamic aerodynamic coefficients. This testing will be combined with CFD to provide higher fidelity aerodynamic databases for implementation in the simulation. A combination of CFD and testing will be continued to refine the heating environments for use in further thermal protection system design.

AEROSHELL DESIGN CONSIDERATIONS FOR HUMAN MISSIONS

An example of the aeroshell used for the aerocapture and EDL for the Mars landers used for human missions is illustrated in Figure 23. This configuration is driven primarily by the large masses and volumes needed for human Mars missions and the aerodynamic characteristics needed for the aeroassist functions. The configuration has no discontinuities in the slope of the outer mold line and provides the needed cargo volume with no on-orbit aeroshell assembly. The aeroshell has the potential to also function as the protective shroud on the launch vehicle. The angle-of-attack during aerocapture and atmospheric entry is 45 to 55 deg to provide a large drag coefficient to minimize the aerodynamic heating and improve the deceleration in the supersonic flight regime in preparation for terminal descent, while providing an acceptable L/D for the aeroassist functions. This L/D results in an acceptable Mars approach corridor even with limited aerodynamic loads to accommodate the flight crew and also provides the aerodynamic maneuverability needed for precision landing. The angle-of-attack is controlled by the location of the system center-of-mass that is located longitudinally at about 50% point and offset about 10% of the body diameter perpendicular to the axis of symmetry. Analytical analysis of the bare airframe dynamics and 6 degree-of-freedom simulations with open loop guidance have demonstrated satisfactory stability and control characteristics of this configuration.

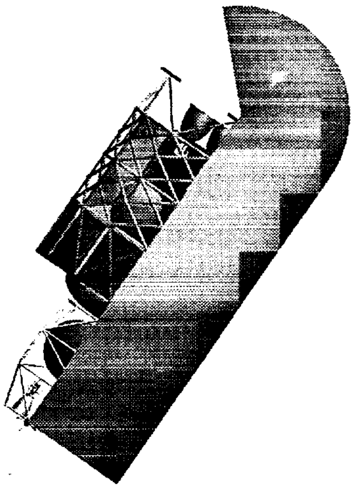

Angle-of-Attack
45 deg Aerocapture
55 deg Aero Entry

Mass – 70 Mt Aerocapture
– 59 Mt Aero Entry
28 ft Diameter, 70 ft Length

Figure 23 Example Aeroshell Configuration for Mars Human Missions

There are two key issues that must be further addressed for human missions. First, the large ballistic coefficient limits the deceleration in the supersonic to subsonic flight regime requiring a significant increase in the deployment envelope for aerodynamic deceleration devices. Second, a parachute system for added low speed deceleration to minimize demands on the propulsion system used for terminal descent is very large.

SUMMARY

A high fidelity 3-DOF simulation has been developed for the 2nd generation lander and has been utilized to assess the baseline performance and assist in further design development. The ETPC guidance algorithm has been demonstrated through high fidelity simulations to provide the aeromaneuvering necessary to meet the precision landing requirements, for adequate available vehicle control authority, with the range of uncertainties in states, atmosphere, aerodynamics, etc. In cases where a trade must be made between the landing footprint objective and safe touchdown, the guidance algorithm demonstrates the ability to sacrifice footprint for safe touchdown. Design requirements for the 2nd generation lander configuration have been developed which define the minimum L/D and maximum M/C_DS required to provide adequate control authority such that the range of errors associated with radiometric navigation and all of the other dispersions can be overcome to meet the landing footprint, parachute deploy conditions and soft touchdown objectives. Many candidate 2nd generation lander configurations have been screened to assess aerodynamic performance, aeroheating environments, and other configuration-specific properties. Based on these results, 2nd generation lander configurations have been developed that meet the L/D and M/C_DS requirements, as well as the additional objectives and requirements for load path, packaging, etc. as defined above. The addition of optical navigation technology significantly improves the robustness of the system toward meeting the landing footprint objectives. The aeroassist technologies developed for the 2nd generation robotic lander will benefit and can be extended to 3rd generation robotic and human missions.

REFERENCES:

1. Thurman, S.W. "Next-Generation EDL System For Mars Landers" LPI Workshop, July, 2000, Houston, TX.

2. Rivellini, T. P., Oritz, G. M. and Steltzner, A. D. "Safe Landing In Extreme Terrain" LPI Workshop, July, 2000, Houston, TX.

3. Carman, G. L., Ives, D. G. and Geller, D. K. "Apollo-Derived Precision Lander Guidance," AIAA Guidance, Navigation, and Control Conf., Aug 1998, Boston, MA, No. 98-4570.

4. Striepe, S. A., Queen, E. M., Powell, R. W., Braun, R. D., Cheatwood, F. N., Aguirre, J. T., Sachi, L. A. and Lyons, D. T. "An Atmospheric Guidance Algorithm Testbed for the Mars Surveyor Program 2001 Orbiter and Lander." AIAA Guidance, Navigation, and Control Conf., Aug 1998, Boston, MA, No. 98-4569.

5. Klumpp, A. R. "Apollo Lunar Descent Guidance" Automatica, Mar 1974, vol. 10, pp.133-146.

6. Bauer, G.L., Cornick, D.E., and Stevenson, R. "Capabilities and Applications of the Program to Optimize Simulated Trajectories (POST)," NASA CR-2770, February 1977.

7. Konopliv, A.S., and Sjogren, W.L. "The JPL Mars gravity field, Mars 50c, based upon Viking and Mariner 9 doppler tracking data," NASA CR-198881, Feb. 1995.

8. Justus, C.G., "Mars Global Reference Atmospheric Model for Mission Planning and Analysis," Journal of Spacecraft and Rockets, Vol. 28, No. 2, pp. 216-221, April-June 1991.

9. Sammonds, R.I., Dickey, R.R., "Effectiveness of Several Control Arrangements on a Mercury-Type Capsule," NASA TM X-579, October, 1961.

10. Peiro, J., Peraire, J., and Morgan, K., "FELISA System Reference Manual and User's Guide," Tech. Rep., University College Swansea Report, 1993.

11. N.R.Merski, "Global Aeroheating Wind Tunnel Measurements Using Improved Two-Color Phosphor Thermography Method," Journal of Spacecraft and Rockets, Vol 36, No. 2, pps 160-170, March/April, 1999.

Acknowledgements: The authors would like to recognize the contributions of EDL team members at JPL, JSC, ARC, NAWC and LaRC. In addition a few special thanks to individuals without whose efforts this paper would not have been possible. Thank you to T.J. Horvath of the Aerothermodynamics Branch of the NASA Langley Research Center, for the LaRC Mach 6 CF4 data on the tab configurations proposed for the Mars Surveyor 2001 Precision Lander. Thank you to N.R. Merski of the Aerothermodynamics Branch of the NASA Langley Research Center, for the aeoheating environment results from the LaRC Mach 6 CF4 test. Thank you to M.L. McMillin of the Vehicle Analysis Branch of the NASA Langley Research Center for the tab geometry figures. Thank you to R.K. Prabhu, a Lockheed Martin employee on-site with the Aerothermodynamics Branch of the NASA Langley Research Center, for the FELISA aerodynamic CFD results. Thank you to M.Schoenenberger of the Vehicle Analysis Branch of the NASA Langley Research Center for the AFE derivative results. Thank you to Scott Striepe of the Vehicle Analysis Branch of the NASA Langley Research Center for the Monte Carlo analysis results.